Settings for Spaceborne 3-D Scattering Tomography of Liquid-Phase Clouds by the CloudCT Mission

Masada Tzabari, Vadim Holodovsky, *Member, IEEE*, Omer Shubi, Eshkol Eytan, Ilan Koren, and Yoav Y. Schechner, *Member, IEEE*

***Abstract*— We introduce a comprehensive method for spaceborne 3-D volumetric scattering-tomography of cloud microphysics, developed for the CloudCT mission. The retrieved microphysical properties are the liquid-water-content (LWC) and effective droplet radius within a cloud. We include a model for a perspective polarization imager and an assumption of 3-D variation of the effective radius. Elements of our work include computed tomography initialization by a parametric horizontally uniform microphysical model. This results in smaller errors than the prior art. The mean absolute errors of the retrieved LWC and effective radius are reduced from 62% and 28% to 40% and 9%, respectively. The parameters of this initialization are determined by a grid search of a cost function. Furthermore, we add viewpoints in the cloudbow region, to better sample the polarized scattering phase function. The suggested advances are evaluated by retrieval of a set of clouds generated by large-eddy simulations.**

***Index Terms*— 3-D scattering-tomography, clouds, initialization, polarization, pySHDOM.**

I. Introduction

STATE-of-the-art remote sensing has information deficiency regarding the 3-D nature of small warm clouds. This is due to two major factors. First, at the spatial resolution of most atmospheric science sensors currently in orbit, these clouds may be below pixel resolution. Second, and more importantly, assumptions of common reconstruction algorithms break down when addressing small clouds. The CloudCT [1] space mission, funded by the European Research Council (ERC), aims to retrieve high-resolution 3-D volumetric microphysical properties of small clouds by means of scattering tomography. The mission confronts classic remote sensing biases [2], [3], [4], [5], [6], [7]. These biases are caused by an assumption of a plane-parallel cloud structure and by clouds being smaller than the spatial resolution that has been traditionally used in Earth observations. The anticipated 3-D retrievals should yield new empirical warm-cloud statistics. The statistics will be used to study cloud trends in changing environmental conditions. Based on these expected studies, improved parameterizations of climate models will be developed.

In CloudCT a formation of ten satellites will capture simultaneously multiview images of cloud fields. These will be analyzed by scattering tomography, based on a 3-D radiative-transfer (RT) solver that includes multiple scattering. Images will be captured in daytime, exploiting solar radiation as the light source. The satellites will be in a low Earth orbit (LEO) of ≈500 km altitude. In each orbit cycle (≈94 min), several cloud-fields will be imaged. The clouds of major interest are small liquid-phase clouds, typically hundreds of meters wide. Therefore, ground resolution should be finer than ≈50 m at nadir.

Classic remote-sensing assumes a plane-parallel geometry [2], [3], [4], [5], [6], [7]. This effectively degenerates, to some extent, 3-D RT to a 1-D form, as if effectively there is neither horizontal heterogeneity nor RT. This assumption is particularly invalid at edges of clouds. This leads to biased retrievals of the cloud microphysics [2], [3], [4], [5], [6], [7]. In particular, this leads to high uncertainties regarding the microphysics and radiative effects of small clouds, regardless of the sensing resolution.

To allow better understanding of microphysics and RT in small clouds, a 3-D retrieval approach is essential. 3-D modeling currently receives growing attention [8], [9], [10], [11]. Levis *et al.* [12], [13], [14], introduced 3-D scattering computed tomography (CT), based on the spherical harmonic discrete ordinate method (SHDOM) for RT [15]. Their method, pySHDOM [16], retrieves cloud properties by fitting multiview light intensity images to a physics-based forward model. This is a generalization of CT to recover scattering by passive sensing, relying only on the Sun as an illumination source.

Scattering-based CT was further developed using vSHDOM [17], for vectorized RT, allowing consideration of polarization [18]. There, cloud properties are retrieved by fitting Stokes vectors. Polarization has advantages for retrieval of the cloud-droplet size distribution [19], [20], [21], [22], [23], [24], [25]. However, these advantages are specifically related to cloud regions where single-scattering may be sensed: mainly one or two optical depths (ODs) into the cloud [19], [26]. This article takes a step beyond the basic principle of cloud tomography, to elements that guide the CloudCT

Manuscript received 13 March 2022; revised 10 July 2022; accepted 24 July 2022. Date of publication 15 August 2022; date of current version 13 September 2022. This work was supported by the European Union's Horizon 2020 Research and Innovation Program under Grant 810370-ERC-CloudCT. *(Masada Tzabari and Vadim Holodovsky are co-first authors.) (Corresponding author: Vadim Holodovsky.)*

Masada Tzabari, Vadim Holodovsky, Omer Shubi, and Yoav Y. Schechner are with the Viterbi Faculty of Electrical and Computer Engineering, Technion-Israel Institute of Technology, Haifa 3200003, Israel (e-mail: masada.tz@campus.technion.ac.il; vholod@technion.ac.il).

Eshkol Eytan and Ilan Koren are with the Department of Earth and Planetary Sciences, Weizmann Institute of Science, Rehovot 7610001, Israel.

Digital Object Identifier 10.1109/TGRS.2022.3198525

This work is licensed under a Creative Commons Attribution 4.0 License. For more information, see https://creativecommons.org/licenses/by/4.0/

mission, considering the mission constraints. The mission will use visible-light (VIS) polarized imagers [27], [28].

A. State-of-the-Art

Two main cloud parameters are usually retrieved from satellite measurements: OD and droplet effective radius (r_e). There are two dominant approaches in remote sensing for retrieving r_e. One is by a bispectral technique developed by Nakajima and King [29], currently used by the operational Moderate Resolution Imaging Spectrometer (MODIS) [30]. It uses VIS or near-infrared (NIR) bands combined with shortwave infrared (SWIR) bands. The retrieval is based on a plane-parallel RT assumption and done per atmospheric column, assuming an independent pixel approximation (IPA) [31]. The finer resolution of MODIS retrievals is 1 km^2 [30].

Studies find significant biases due to the plane-parallel assumption [2], [3], [4], [5], [6]. Marshak *et al.* [5] explore r_e uncertainty stemming from cloud horizontal inhomogeneity. They examine retrievals from data at pixel resolution on the scale of kilometers, as in MODIS. They point to two main findings: a) Subpixel heterogeneity leads to an underestimation of r_e. b) Heterogeneity in a scale larger than a pixel leads to an overestimation of a domain-averaged r_e. They show by simulation an overall positive bias of 60% for cumulus clouds. Grosvenor *et al.* [32] emphasize the significance of more accurate r_e retrievals, as they dominate the uncertainty of the cloud droplet number concentration.

A second sensing approach uses polarized radiance measurements. Polarized reflectance is affected by the polarized scattering phase function of droplets, which has strong features in the cloudbow scattering angles ($\approx$135°–165°). The phase function is sensitive to the droplet size distribution. Therefore, r_e may be retrieved. This approach was demonstrated by the polarization and directionality of the Earth's reflectances (POLDER) instrument [19], [21] and later spaceborne missions [33], [34], [35]. POLDER has ground resolution of $\approx 6 \times 7$ km^2 at nadir [36]. Recent methods suggest side-scanning to retrieve vertical profiles of cloud droplet properties [37], [38]. Alexandrov *et al.* [38] demonstrate fitting of high-resolution side-scanning measurements, by the airborne research scanning polarimeter (RSP).

Fu *et al.* [7] present a thorough comparison of retrievals based on data from the 2019 Cloud, Aerosol, and Monsoon Processes Philippines Experiment (CAMP2 Ex). Bispectral and polarimetric retrievals are compared using data from MODIS, RSP, and *in situ* measurements. Fu *et al.* [7] present a positive bias of 50%, mainly due to 3-D radiative effects.

Matar *et al.* [6] demonstrate dual-wavelength retrievals using multiview polarized measurements, taken by the airborne Observing System Including PolaRization in the Solar Infrared Spectrum (OSIRIS). Here too, analysis used the plane-parallel assumption. They emphasize the significance of a heterogeneous column model, pointing to an error of more than 10% solely due to a homogeneous column assumption.

Liquid-water-content (LWC) can be retrieved using cloud radar reflectivity. Ebell *et al.* [39] estimate errors in retrieval of the LWC to be larger than 60% for shallow nondrizzling clouds. Zhu *et al.* [40] estimate the uncertainty in radar dual-wavelength retrievals of the LWC. They estimate an uncertainty of between 0.1 (g/cm^3) and 0.65 (g/cm^3) for shallow clouds, decreasing with cloud thickness.

Operational methods do not consider 3-D RT effects, nor do they perform 3-D volumetric retrieval of cloud parameters. Levis *et al.* [18] derive and define a polarimetric 3-D scattering tomography method for retrieval of cloud droplet microphysics, using multiview multispectral image measurements, based on vSHDOM. This method is the basis for our current work. They present demonstrations based on the Airborne Multiangle SpectroPolarimetric Imager (AirMSPI) [18], [41]. Doicu *et al.* [42] presents another method for tomographic cloud retrievals, also based on SHDOM. Doicu *et al.* [43] further develop an algorithm based on an adjoint method for gradient computation.

Forster *et al.* [26] have recently explored the use of 3-D scattering tomography, based on data from MODIS [44] and the Multiangle Imaging SpectroRadiometer (MISR) [45]. For 3-D RT, Forster *et al.* [26] use the 3-D Monte-Carlo Code of the Physically Correct Tracing of Photons in Cloudy Atmospheres (MYSTIC) [11], [46], [47]. Forster *et al.* [26] examine a basic limitation of retrieval. They explore a region of the cloud in which microphysical properties cannot be resolved by scattering tomography, termed the *veiled core*. Their demonstration, however, was without considering polarization.

CloudCT offers very different spaceborne retrievals than the operational state of the art. As in [18], CloudCT suggests 3-D retrieval of cloud microphysics using scattering tomography. Operational spaceborne instruments designed for global coverage, have retrieval spatial resolution that is coarse relative to the clouds of interest. CloudCT will image clouds with spatial resolution of finer than 50 m, and retrieve at volumetric resolution of $\approx 50 \times 50 \times 50$ m^3.

In this article, we present a comprehensive method for retrieval, highlighting adjustments and improvements which we implement. We make advances needed for realistic spaceborne perspective optical imaging. We model the imager as having a polarized sensor as in [48]. We introduce a new method for initialization of the retrieval medium, based on a parameterized horizontally uniform model. This medium is updated by an optimization process.

II. Background

A. Parameter Definition

Air molecular density is assumed to be known. Thus, we do not try to retrieve air density. By cloud tomography, we retrieve the cloud-droplet microphysics. We assume small warm clouds, i.e., liquid-phase clouds. The droplets have spherical geometry[1] of variable radius values r. One of the unknowns is the 3-D distribution of the LWC. Let the droplet size distribution at a volume element be $n(r)$ $(1/\mu\text{m}) \cdot (1/\text{m}^3)$. The droplet size distribution is

[1]This is a common approximation for cloud-droplets, where Mie theory is used to describe light scattering.

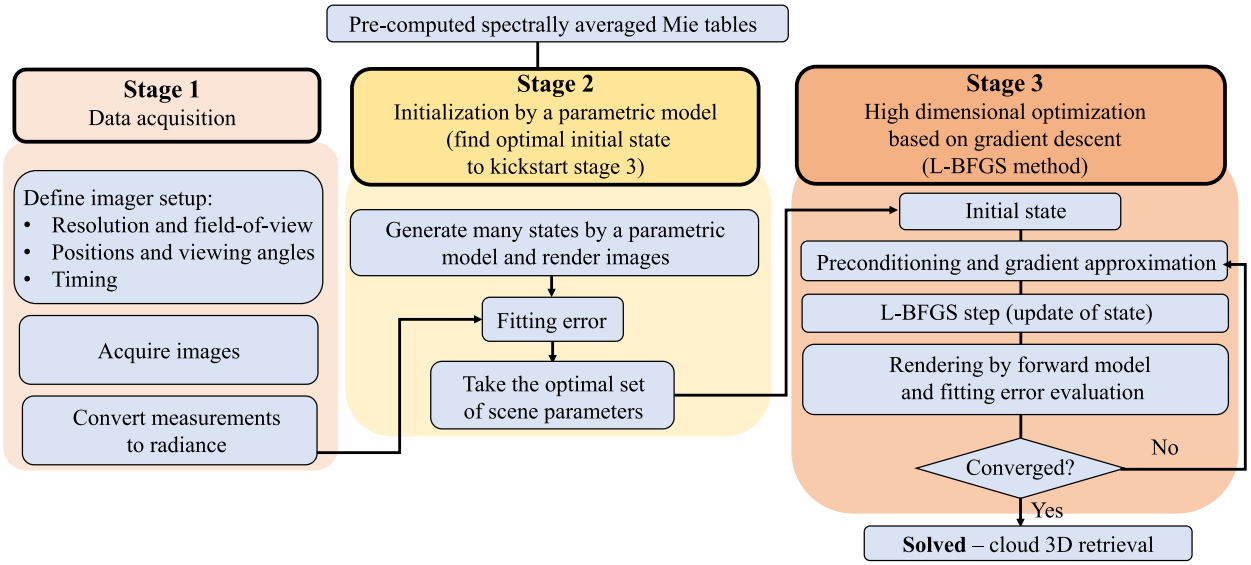

Fig. 1. Overview of the retrieval method (see Section II-B).

parameterized by a gamma distribution model as in [49]. The LWC is

$$\mathrm{LWC} = \frac{4}{3}\pi\rho_w \int_r r^3 n(r)dr \qquad \left[\frac{\mathrm{g}}{\mathrm{m}^3}\right] \tag{1}$$

where $\rho_w = 1$ (g/cm^3) is the water density. The effective radius r_e μm is defined [49] by

$$r_e = \frac{\int(\pi r^2) r n(r)dr}{\int(\pi r^2) n(r)dr}. \tag{2}$$

The extinction coefficient is

$$\beta = \int n(r) Q \pi r^2 \tag{3}$$

where Q is the extinction efficiency. For Mie scattering at VIS, $Q \approx 2$. Therefore, there is a relation between β, r_e, and LWC

$$\beta = \frac{3}{2}\frac{\mathrm{LWC}}{r_e \rho_w} \qquad \left[\frac{1}{\mathrm{m}}\right]. \tag{4}$$

The OD along a path $\boldsymbol{x}$ is defined as $\int_{\boldsymbol{x}} \beta(x)dx$. In this article, we focus on the retrieval of the LWC and r_e as in [18].

B. Retrieval Overview

Retrieval includes the following stages (See Fig. 1).

1) Stage 1) *Data acquisition:* This stage consists of the imager setup definition, optics, and camera positions. With these settings, a set of *measured images* is acquired. The measured images in our case are partially polarized intensity images. From these raw images, spatial maps of the Stokes vector components are calculated. This stage is currently simulated.
2) Stage 2) *Initialization:* Definition of an initial state of the sought variables. This kick-starts iterative optimization, to be done in Stage 3. The initialized state of the medium may be set in various ways, e.g., it may be entirely null. However, in general, the more similar the initialized medium is to the true state, the better and faster the optimization is.
3) Stage 3) *Optimization based on gradient descent:* In this stage, a set of *modeled images* is rendered by a forward model.[2] The forward model solves the 3-D RT equation using SHDOM [10], [50]. The forward model uses the initialized state medium and then updates the modeled medium through an iterative optimization process. The optimization seeks the 3-D fields **LWC** and $\boldsymbol{r}_e$, which lead to the best fit of modeled images to measured images. This is the essence of CT. Many viewpoints sample multiple ray paths through each volume-unit, providing a variety of data for CT. In our case, the radiance is partially polarized. Thus, each measured pixel is associated with Stokes vector components. Classic CT uses simple straight integrated paths. However, in our case, scattering dominates the signal, thus our CT does not rely on straight paths but on 3-D RT.

Let the number of viewpoints be N_{view}. Let the number of pixels of each view be N_{pixels}. The number of measurements is $N_{\mathrm{meas}} = N_{\mathrm{view}} N_{\mathrm{pixels}}$. The set of unknowns is $\boldsymbol{\Theta} = [\mathbf{LWC}, \boldsymbol{r}_e]$. A cost function is defined according to the difference between modeled values and measurements. In general

$$\mathrm{cost}(\boldsymbol{\Theta}) = \frac{1}{2}\sum_{k=1}^{N_{\mathrm{meas}}} (\mathrm{modeled}_{\boldsymbol{\Theta}}[k] - \mathrm{measured}[k])^2. \tag{5}$$

Here, $\mathrm{modeled}_{\boldsymbol{\Theta}}$ is the result of the image formation (forward) model, which is RT. The estimated values of the unknowns are

$$\hat{\boldsymbol{\Theta}} = \arg\min_{\boldsymbol{\Theta}}(\mathrm{cost}[\boldsymbol{\Theta}]). \tag{6}$$

[2]The forward model is the image formation model. It involves 3-D RT with multiple scattering. The 3-D RT equation (RTE) yields the radiance value in a pixel. It is solved numerically and iteratively by the pySHDOM [16].

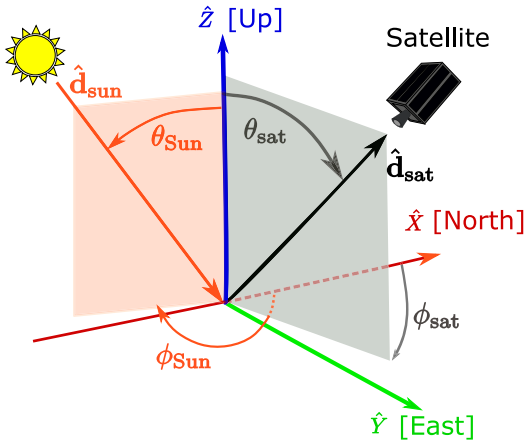

Fig. 2. TE local Cartesian coordinate system ENU, and zenith and azimuth angles of the Sun and satellite. The direction of the Sun is indicated by $\hat{\mathbf{d}}_{\text{sun}}$. The satellite viewing direction is indicated by $\hat{\mathbf{d}}_{\text{sat}}$.

The derivatives of the RT forward model with respect to $\boldsymbol{\Theta}$ are calculated by pySHDOM [16] and their expressions are presented in [18]. These derivatives are used to express the gradient of the RT forward model. Minimization of the cost function is by the Limited memory Broyden–Fletcher–Goldfarb–Shanno algorithm (L-BFGS) method which is a part of pySHDOM [16].

C. Retrieval Quality Measure

Let $\mathbf{LWC}$ and $\boldsymbol{r}_e$ be the ground-truth fields. Let $\widehat{\mathbf{LWC}}$ and $\widehat{\boldsymbol{r}_e}$ be the corresponding estimated 3-D fields. The quality of a retrieval is quantitatively estimated per cloud i by the relative error ϵ [18]

$$\epsilon^{(i)}_{\mathbf{LWC}} = \frac{\|\widehat{\mathbf{LWC}}^{(i)} - \mathbf{LWC}^{(i)}\|_1}{\|\mathbf{LWC}^{(i)}\|_1}, \quad \epsilon^{(i)}_{\boldsymbol{r}_e} = \frac{\|\widehat{\boldsymbol{r}_e}^{(i)} - \boldsymbol{r}_e^{(i)}\|_1}{\|\boldsymbol{r}_e^{(i)}\|_1}. \tag{7}$$

For the retrieval of a set of N_c separate clouds, a mean relative error is

$$\overline{\epsilon_{\mathbf{LWC}}} = \frac{1}{N_c}\sum_{i=1}^{N_c} \epsilon^{(i)}_{\mathbf{LWC}}, \quad \overline{\epsilon_{\boldsymbol{r}_e}} = \frac{1}{N_c}\sum_{i=1}^{N_c} \epsilon^{(i)}_{\boldsymbol{r}_e}. \tag{8}$$

III. Data Acquisition

Stage 1 of each retrieval is data acquisition (see Section II-B and Fig. 1). This stage requires definition of the imager specifications, positions, and viewing angles. These need to be defined to suit retrieval demands. The imaging is passive: The only source is the Sun. The retrieval requires simultaneous multiview images of a single cloud field, with high overlap between the multiviews.

The temporal resolution of the retrieval depends on the frame rate of data acquisition, while high synchronicity is achieved. If synchronicity is not practical, temporal accumulation of data of up to ≈30 s may be applied [51].

A. Coordinate Systems

In this section, we detail several coordinate systems which are referred to throughout this article. The following points explain these coordinate systems. Points 1 and 2 refer to coordinate systems which are used to express a 3-D position in the world. Point 3 is the camera coordinate system. Points 4–6 are used as the reference frames of a Stokes vector.

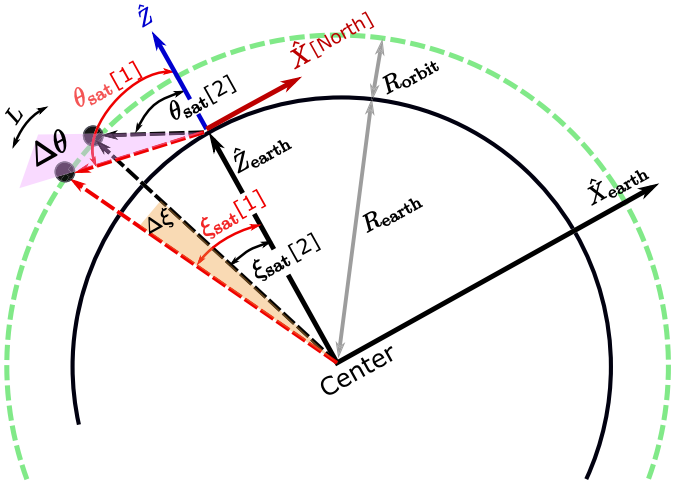

Fig. 3. Topocentric Earth (TE) and Earth-centered (EC) coordinate systems, as well as the satellite zenith angles in these coordinate systems.

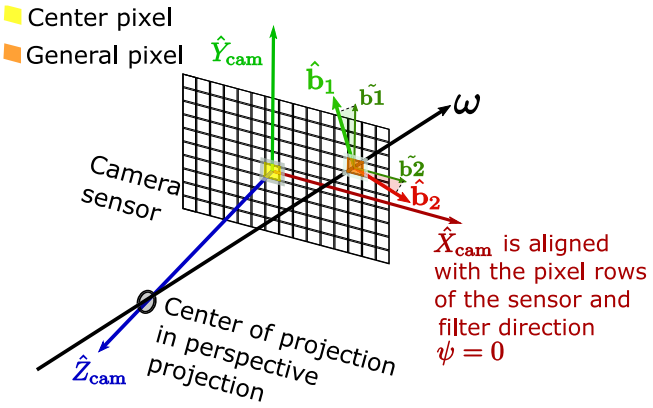

Fig. 4. Camera coordinate system and a pixel coordinate system.

1) *The topocentric Earth (TE) coordinate system.* The origin of the TE system is on the Earth's surface. The TE coordinate system is expressed as East, North, Up (ENU) (Fig. 2). In our convention, the east axis is labeled $\hat{\boldsymbol{Y}}$, the north $\hat{\boldsymbol{X}}$, and the zenith $\hat{\boldsymbol{Z}}$.
2) *The Earth-centered (EC) coordinate system.* The origin of the EC system is at the Earth's center, as shown in Fig. 3. The axes of this system are $\hat{\boldsymbol{X}}_{\text{earth}}$, $\hat{\boldsymbol{Y}}_{\text{earth}}$, $\hat{\boldsymbol{Z}}_{\text{earth}}$. Axis $\hat{\boldsymbol{X}}_{\text{earth}}$ is parallel to $\hat{\boldsymbol{X}}$, $\hat{\boldsymbol{Y}}_{\text{earth}}$ is parallel to $\hat{\boldsymbol{Y}}$ and $\hat{\boldsymbol{Z}}_{\text{earth}}$ is parallel to $\hat{\boldsymbol{Z}}$. With respect to the EC system, the center of the TE system is at $Z_{\text{earth}} = R_{\text{earth}}$, $Y_{\text{earth}} = 0$, $X_{\text{earth}} = 0$, as shown in Fig. 3. The relation between EC and TE is further detailed in Appendix I.
3) *The camera coordinate system.* The origin of the system is at the center pixel of the sensor, as shown in Fig. 4. The axes of this system are $\hat{\boldsymbol{X}}_{\text{cam}}$, $\hat{\boldsymbol{Y}}_{\text{cam}}$, $\hat{\boldsymbol{Z}}_{\text{cam}}$. Axes $\hat{\boldsymbol{X}}_{\text{cam}}$ and $\hat{\boldsymbol{Y}}_{\text{cam}}$ are parallel to the pixel rows and columns of the imager sensor, respectively. Axis $\hat{\boldsymbol{Z}}_{\text{cam}}$ aligns with the optical axis of the camera. The satellite

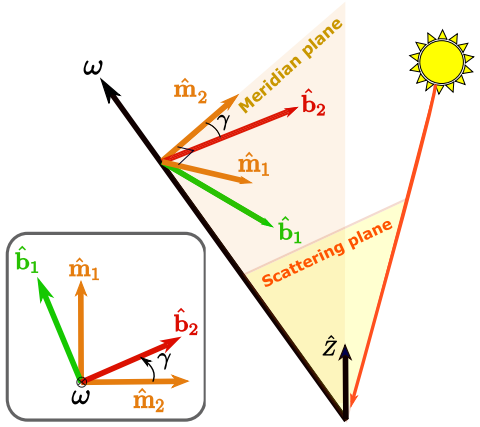

Fig. 5. Meridian and pixel coordinate systems, and the scattering plane. In the 2-D illustration, $\boldsymbol{\omega}$ is directed into the page.

viewing direction $\hat{\mathbf{d}}_{\text{sat}}$ (from field of view toward satellite), is equal to $-\hat{\boldsymbol{Z}}_{\text{cam}}$ (see Fig. 2).

4) *The meridian coordinate system*. As shown in Fig. 5, the meridian plane contains the viewing direction $\boldsymbol{\omega}$ (from the observed object toward the camera) and the zenith $\hat{\boldsymbol{Z}}$ at the viewed point on Earth. In the meridian coordinate system, two orthogonal unit vectors are, respectively, defined [18], [52] by

$$\hat{\mathbf{m}}_1 = \hat{\boldsymbol{Z}} \times \boldsymbol{\omega}, \quad \hat{\mathbf{m}}_2 = \boldsymbol{\omega} \times \hat{\mathbf{m}}_1. \tag{9}$$

The meridian coordinate system is a right-handed Cartesian coordinate system defined by $\hat{\mathbf{m}}_1$, $\hat{\mathbf{m}}_2$ and $\boldsymbol{\omega}$ (see Fig. 5).

5) *The pixel coordinate system*. A right-handed Cartesian coordinate system defined by $\hat{\mathbf{b}}_1$, $\hat{\mathbf{b}}_2$ and $\boldsymbol{\omega}$ (see Figs. 4 and 5), where

$$\hat{\mathbf{b}}_2 = \boldsymbol{\omega} \times \hat{\boldsymbol{Y}}_{\text{cam}}, \quad \hat{\mathbf{b}}_1 = \hat{\mathbf{b}}_2 \times \boldsymbol{\omega}. \tag{10}$$

Let $\tilde{\mathbf{b}}_1$ and $\tilde{\mathbf{b}}_2$ be the normalized (to unit vector) projections of $\hat{\mathbf{b}}_1$ and $\hat{\mathbf{b}}_2$ on the camera plane, respectively. The vector $\tilde{\mathbf{b}}_2$ aligns with $\hat{\boldsymbol{X}}_{\text{cam}}$. The vector $\tilde{\mathbf{b}}_1$ does not align with $\hat{\boldsymbol{Y}}_{\text{cam}}$ for most of the pixels. There is a slight deviation which can be expressed as

$$\Sigma = \left\| \cos^{-1}(\tilde{\mathbf{b}}_1 \cdot \hat{\boldsymbol{Y}}_{\text{cam}}) \right\|. \tag{11}$$

As an example, for a camera with a $\approx 5°$ field-of-view (FOV), as intended for the CloudCT mission, $\Sigma \leq 0.143°$. Therefore, we assume the Stokes vector in the camera coordinate system is practically identical to that which is expressed in the pixel coordinate system.

6) *The Scattering plane*. The scattering plane (Fig. 5) contains the viewing direction $\boldsymbol{\omega}$ and the Sun light propagation direction $\hat{\mathbf{d}}_{\text{sun}}$ (see Fig. 2). This plane is usually referenced when considering polarization caused by single scattering in the atmosphere. PySHDOM is based on multiple scattering. When the RT model simulates multiple scattering, it is common to represent polarization in the meridian coordinate system. However, the cloudbow (described below) angular region is defined in the scattering plane.

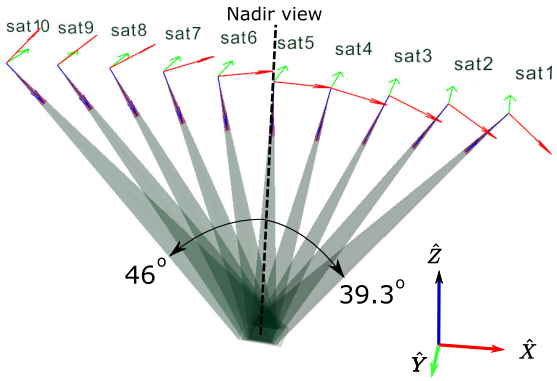

Fig. 6. Imaging setup of ten satellites at 500 km orbit, as described in Section III-B.

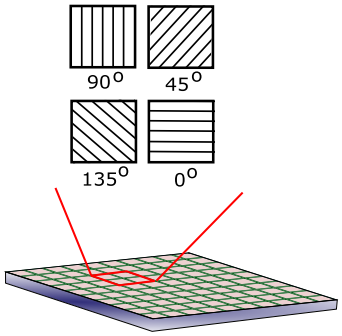

Fig. 7. Wire-grid polarizing filters in a block of pixels in Sony Polarsens sensor.

B. Imaging Setup

Imagers are positioned by a satellite formation. The satellites' configuration is constant in all our demonstrations. A set of ten imagers in separate satellites is considered. The satellites are assumed to be in a trailing formation (*string of pearls*), moving northward consecutively, as illustrated in Fig. 6. The altitude of the satellites is $R_{\text{orbit}} = 500$ km. The uniform distance between each pair of neighboring satellites is 100 km, on the orbit arc. The viewing angles are between $-46°$ and $39.3°$ relative to the zenith.

The imager used in the demonstrations herein is a monochrome polarization camera, having a Sony IMX250MZR sensor, and a spectral filter. The Sony sensor [48] has four types of wire-grid polarizing filters which are formed on the chip in blocks of four pixels, as illustrated in Fig. 7. Each filter in a block has a polarization angle $\psi \in [0°,45°,90°,135°]$, relative to $\hat{\boldsymbol{X}}_{\text{cam}}$ in the image-sensor coordinate system (Fig. 4).

High spatial resolution is needed for retrievals at high volumetric resolution. State-of-the-art remote-sensing retrievals are restricted by radiative smoothing [53], due to unresolved horizontal fluxes. These fluxes have been neglected in traditional methods due to the assumption of a plane parallel cloud structure. A 3-D RT model obviates this limitation. Therefore, the only limitation we consider is that of the imaging optics. In the demonstration herein, the imaging payload optics lead to nadir resolution of 20 m. Tomography relies on integrated measurements along multiangular ray paths.

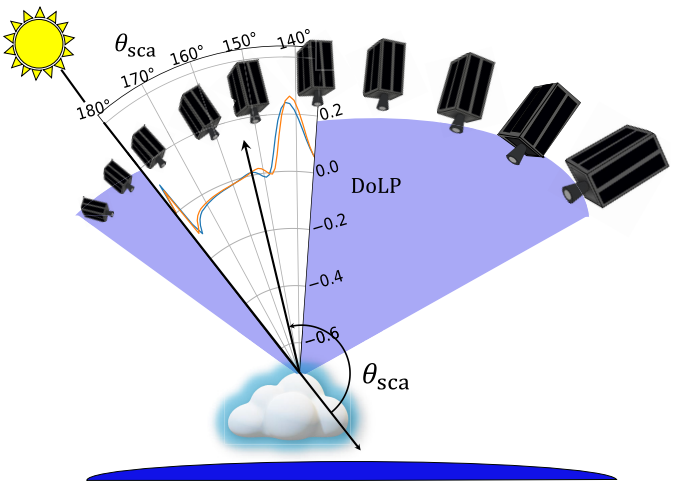

Fig. 8. Scattering angle in the scattering plane. In this illustration, the scattering plane encapsulates the satellite formation. The curves are the DoLP of the scattered radiation as a function of the scattering angle, for droplet size-distributions of $r_e = 8\ \mu m$ (blue) and $r_e = 10\ \mu m$ (orange), assuming an effective variance of $v_e = 0.1$.

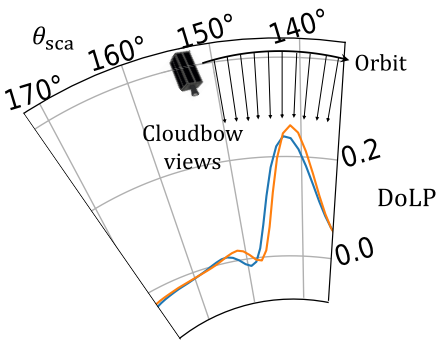

Fig. 9. Focus on Fig. 8, illustrating scattering angles for cloudbow-scan sampling.

Therefore, wide-angle views, despite having lower resolution at high off-nadir angles, improve retrievals.

Typically, a payload swath is defined. Here, we consider the FOV, as we do not focus on pushbroom imaging along a flight path, but on simultaneous multiview 2-D projections. The sensor considered here has 2448×2048 pixels. At 500 km orbit, the corresponding FOV is $\sim 49 \times 41$ km^2 on the ground at nadir. The imager uses a red waveband channel, between 620 and 670 nm. There, absorption by water droplets is negligible, and Rayleigh scattering by air molecules is relatively low. This reduces the airlight. We currently consider a single waveband. We have found by simulations (not presented here) that additional wavebands in the VIS to NIR provide no significant advantage to retrieval of cloud microphysics.

C. Cloudbow-Scan

Polarization of Mie scattered light is significant mostly in a specific range of scattering angles known as the cloudbow. The scattering angle θ_{sca} is the angle between the Sun irradiation direction ($\hat{\mathbf{d}}_{sun}$) and a line of sight from a cloud ($\boldsymbol{\omega}$), in the scattering plane (See Figs. 5 and 8. See also Eqs. (37), (38), and (40) in Appendix II). The cloudbow is mostly in the range $\approx 135° \leq \theta_{sca} \leq 165°$. The polarization depends on the droplet size distribution. In the cloudbow domain, the degree of linear polarization (DoLP) is highly sensitive to r_e, as long as the effective variance is low [21]. In order to better exploit the information of polarization, a cloudbow-scanning principle is integrated into the process.

Images would be acquired, without changing the number of imagers. To achieve this, one or two satellites take a sequence of images of the cloud field, while in orbital motion, as illustrated in Fig. 9. The cloudbow is sampled per $\sim 1.5°$ in θ_{sca}, which is a realistic assumption for satellite attitude control. The outcome is a set of additional satellite views in the cloudbow angular range. The imager which executes the scanning is chosen according to the scattering angles it is positioned to view. Therefore, the chosen imager depends on the solar illumination direction. The method for choosing the most suitable satellite for the task is detailed in Appendix II. In the setup which is described in Section III-B (see Fig. 6), the satellite which scans the cloudbow is satellite number 9. In the simulations presented in this article, a single imager captures ten additional views within the scattering angles of $\approx 135° \leq \theta_{sca} \leq 150°$. On average, we find the cloudbow-scan decreases the mean errors $\overline{\epsilon_{\mathbf{LWC}}}$ and $\overline{\epsilon_{r_e}}$ by 2% and 1%, respectively. We find this is a consistent improvement. However, further sensitivity studies may improve the choice of scanned scattering angles and resolution.

Appendix II describes the calculations of the time-scale for the cloudbow-scan. The time-scale may reach ≈ 30 s. As demonstrated by [51], this is an acceptable time scale regarding evolution of cloud droplet size.

D. Conversion of Measurements to Stokes Vectors

Measurement readouts are represented as grayscale values. There is a linear relation between grayscale levels and photo-electrons detected at sensor pixels (See Appendix III). This section describes the conversion of the expected number of measured photo-electrons to Stokes vector components (radiance units) in the meridian coordinate systems (see Section III-A).[3] The pipeline of the conversion is illustrated in Fig. 10.

Assume a polarization sensor, as described in Section III-B (see Fig. 7). To allow evaluation of the Stokes vector per sensor pixel, demosaicing is used [54], [55]. This way, each image pixel k is associated with four expected numbers of measured photo-electrons at a pixel, $N_{\psi}^{\text{measured}}[k]$ using each polarizer angle ψ. Conversion of $N_{\psi}^{\text{measured}}[k]$ to radiance per pixel k is done by multiplication by a factor A (see Appendix III), where

$$I_{\psi}^{\text{measured}}[k] = A N_{\psi}^{\text{measured}}[k]. \tag{12}$$

The radiance vector $\boldsymbol{I}^{\text{measured}}[k]$ contains all radiance components $I_{\psi}^{\text{measured}}[k]$.

[3]Note that pySHDOM produces the Stokes vector components in the meridian coordinate system.

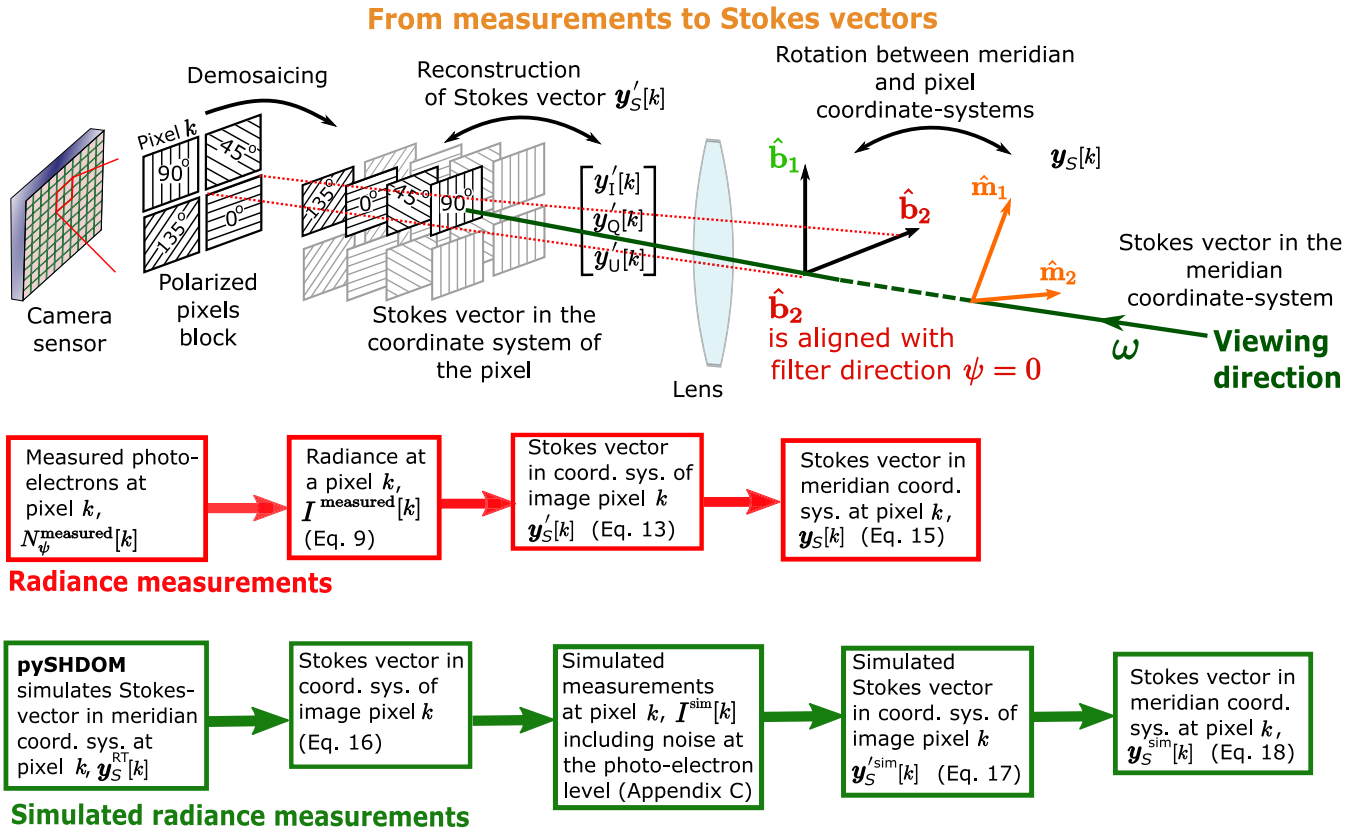

Fig. 10. Pipeline of conversions of radiance measurements (red) or simulated radiance measurements (green) to Stokes vectors.

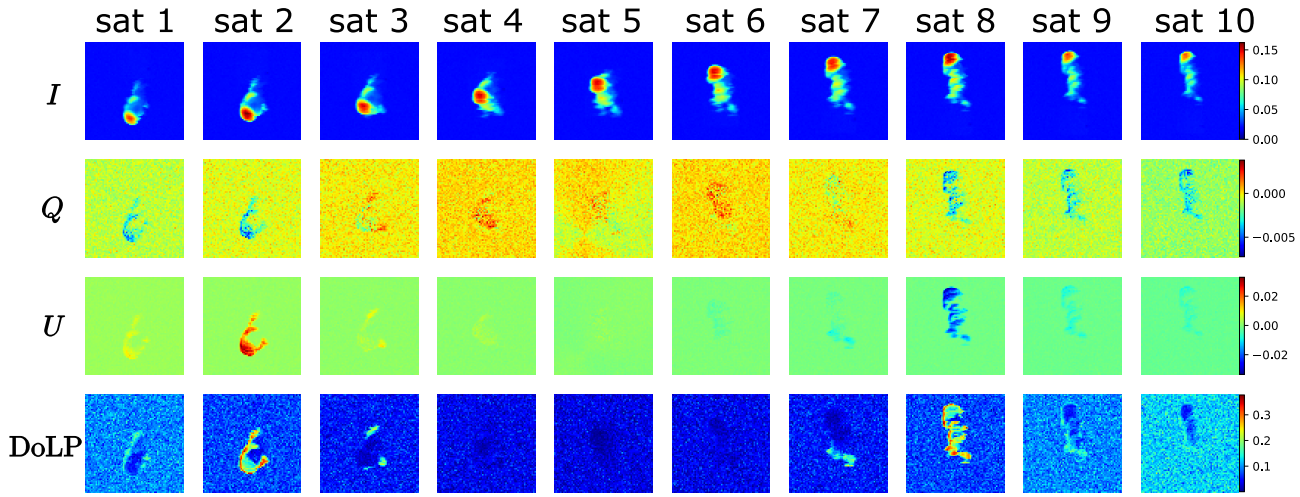

Fig. 11. Simulated (normalized) radiance I, Stokes elements Q and U, and the DoLP, in the meridian coordinate system, as viewed by the satellite setup described in Fig. 6. The DoLP is visibly more noisy than the radiance. Notice the high values of DoLP viewed by sat 2 and 8. They correspond to cloudbow scattering angles.

For a linear polarizer at angle ψ, the Mueller Matrix is

$$\mathbf{M}_{\text{pol}}(\psi) = \frac{1}{2}\begin{bmatrix} 1 & \cos 2\psi & \sin 2\psi \\ \cos 2\psi & \cos^2(2\psi) & \sin(2\psi)\cos(2\psi) \\ \sin 2\psi & \sin(2\psi)\cos(2\psi) & \sin^2(2\psi) \end{bmatrix}. \tag{13}$$

The pixel intensity readout includes only the first element of the Stokes vector. This corresponds to the first row of $\mathbf{M}_{\text{pol}}(\psi)$. Let $\boldsymbol{y}'_S[k]$ be the unknown Stokes vector of pixel k in the $(\hat{\mathbf{b}}_{1k}, \hat{\mathbf{b}}_{2k})$ pixel coordinate system. According to (13), the radiance readouts per pixel are related to this Stokes vector according to

$$\boldsymbol{I}^{\text{measured}}[k] = \mathbf{G}\,\boldsymbol{y}'_S[k] \tag{14}$$

where

$$\mathbf{G} = \frac{1}{2}\begin{bmatrix} 1 & \cos 2\psi_1 & \sin 2\psi_1 \\ 1 & \cos 2\psi_2 & \sin 2\psi_2 \\ 1 & \cos 2\psi_3 & \sin 2\psi_3 \\ 1 & \cos 2\psi_4 & \sin 2\psi_4 \end{bmatrix} = \frac{1}{2}\begin{bmatrix} 1 & 1 & 0 \\ 1 & 0 & 1 \\ 1 & -1 & 0 \\ 1 & 0 & -1 \end{bmatrix}. \tag{15}$$

Hence, the Stokes vector at pixel k can be calculated from $\boldsymbol{I}^{\text{measured}}[k]$ as

$$\boldsymbol{y}'_S[k] = [\mathbf{G}^\top \mathbf{G}]^{-1} \mathbf{G}^\top \boldsymbol{I}^{\text{measured}}[k]. \tag{16}$$

Pixel k corresponds to a viewing direction $\boldsymbol{\omega}_k$, a pixel coordinate axis $\hat{\mathbf{b}}_{2k}$, and a meridian coordinate axis $\hat{\mathbf{m}}_{2k}$. The angle between $\hat{\mathbf{m}}_{2k}$ and $\hat{\mathbf{b}}_{2k}$ is γ_k (Section III-A, points 4, 5). Let $\mathbf{M}_{\text{rot}}(\gamma_k)$ be the Mueller matrix of rotation by an angle γ_k [56]

$$\mathbf{M}_{\text{rot}}(\gamma_k) = \begin{bmatrix} 1 & 0 & 0 \\ 0 & \cos(2\gamma_k) & \sin(2\gamma_k) \\ 0 & -\sin(2\gamma_k) & \cos(2\gamma_k) \end{bmatrix}. \tag{17}$$

The vector $\boldsymbol{y}'_S[k]$ is then rotated from the pixel coordinate system to the meridian coordinate system (see Section III-A, and Fig. 5) by

$$\boldsymbol{y}_S[k] = \begin{bmatrix} y_I[k] \\ y_Q[k] \\ y_U[k] \end{bmatrix} = \mathbf{M}_{\text{rot}}^{-1}(\gamma_k) \boldsymbol{y}'_S[k]. \tag{18}$$

E. Simulated Measurements

In our demonstration, radiance measurements are simulated (see Fig. 10, green pipeline). An RT model renders the Stokes vector reaching a pixel, $\boldsymbol{y}_S^{\text{RT}}[k]$, in the meridian coordinate system.

The conversion of $\boldsymbol{y}_S^{\text{RT}}[k]$ to measured intensities in the pixel coordinate system is by simulation of rotation and transfer through pixelated polarizers, as follows:

$$\boldsymbol{I}^{\text{sim}}[k] = \mathbf{G}\, \mathbf{M}_{\text{rot}}(\gamma_k) \boldsymbol{y}_S^{\text{RT}}[k]. \tag{19}$$

The RT model does not consider imager noise. Noise needs to be included in the radiance values, in the pixel coordinate system. Noise is thus introduced to $\boldsymbol{I}^{\text{sim}}[k]$ (see Appendix III). The simulated Stokes vector measurement $\boldsymbol{y}_S'^{\text{sim}}[k]$ in the pixel coordinate system is then retrieved by

$$\boldsymbol{y}_S'^{\text{sim}}[k] = \begin{bmatrix} y_I'^{\text{sim}}[k] \\ y_Q'^{\text{sim}}[k] \\ y_U'^{\text{sim}}[k] \end{bmatrix} = [\mathbf{G}^\top \mathbf{G}]^{-1} \mathbf{G}^\top \boldsymbol{I}^{\text{sim}}[k]. \tag{20}$$

Then, $\boldsymbol{y}_S^{\text{sim}}[k]$ is obtained by rotation of $\boldsymbol{y}_S'^{\text{sim}}[k]$ back to the meridian coordinate system by

$$\boldsymbol{y}_S^{\text{sim}}[k] = \mathbf{M}_{\text{rot}}^{-1}(\gamma_k) \boldsymbol{y}_S'^{\text{sim}}[k]. \tag{21}$$

Note that if no noise were applied

$$\begin{aligned} \boldsymbol{y}_S^{\text{sim}}[k] &= \mathbf{M}_{\text{rot}}^{-1}(\gamma_k) [\mathbf{G}^\top \mathbf{G}]^{-1} \mathbf{G}^\top \mathbf{G}\, \mathbf{M}_{\text{rot}}(\gamma_k) \boldsymbol{y}_S^{\text{RT}}[k] \\ &= \boldsymbol{y}_S^{\text{RT}}[k]. \end{aligned} \tag{22}$$

Simulated Stokes vector images and corresponding images of the DoLP are presented in Fig. 11.

IV. Initialization

This section describes Stage 2 of the retrieval (see Section II-B and Fig. 1): There is a need to define a medium (3-D fields of the **LWC** and $\boldsymbol{r}_e$) which initializes the optimization of Stage 3. The initialization method sets model parameters, denoted $\boldsymbol{\Phi}$.

A prior initialization method [18], assumes a simple homogeneous model, in which the entire medium is defined by initialization parameters $\boldsymbol{\Phi} = [\text{LWC}_0, r_{e0}]$. It specifically assumes values $\boldsymbol{\Phi} = \left[\text{LWC}_0 = 0.01\ (\text{g/m}^3), r_{e0} = 12\ \mu\text{m}\right]$. We denote this first method as $\text{H}_{\text{Typical}}$. In addition to the homogeneous model, we describe a horizontally homogeneous parametric cloud model. The parameter values used for each initialization are found by preoptimization of an initial cost function, as we describe. We emphasize that these models are suggested strictly for Stage 2. Once initialized, the optimization in Stage 3 is no longer restricted to either a homogeneous or a horizontally homogeneous assumption.

A. Monotonous Model

Let Z_0 be the cloud-base height. The value of Z_0 can be evaluated by methods of space-carving [57]. Assume the initial cloud model has vertical monotonic profiles of **LWC** and $\boldsymbol{r}_e$ at altitude $Z \geq Z_0$ within a cloud. Following [58], set:

$$\mathbf{LWC} = \alpha_l (Z - Z_0) + \text{LWC}_{\text{min}}, \tag{23}$$

$$\boldsymbol{r}_e = \alpha_r (Z - Z_0)^{\frac{1}{3}} + \boldsymbol{r}_{e_{\text{min}}}. \tag{24}$$

Here, α_l and α_r are parameters of the **LWC** and $\boldsymbol{r}_e$, respectively. Thus, $\boldsymbol{\Phi} = [\alpha_l, \alpha_r]$. We set $\text{LWC}_{\text{min}} = 0.0001\ (\text{g/m}^3)$, $r_{e_{\text{min}}} = 2.5\ \mu\text{m}$. These settings are tested on large-eddy-simulation (LES) cloud data and found suitable for steady-state cumulus convection.

B. Optimal Parameters

For a set of possible initialization methods presented here, the parameters $\boldsymbol{\Phi}$ are found by a small (two unknowns) minimization of a cost function. Because this is a small problem, minimization is achieved by a grid search. We follow the notations of [18]. Two cost functions are considered for polarized imaging. Based on a scene characterized by initialization parameters $\boldsymbol{\Phi}$, let $[I(\boldsymbol{\Phi})[k], Q(\boldsymbol{\Phi})[k], U(\boldsymbol{\Phi})[k]]^\top$ be the modeled Stoke vector components of pixel k. The errors of the components are

$$D_{\text{radiance}}(\boldsymbol{\Phi}) = \frac{1}{2} \sum_{k=1}^{N_{\text{meas}}} \{I(\boldsymbol{\Phi})[k] - y_I[k]\}^2 \tag{25}$$

$$D_Q(\boldsymbol{\Phi}) = \frac{1}{2} \sum_{k=1}^{N_{\text{meas}}} \{Q(\boldsymbol{\Phi})[k] - y_Q[k]\}^2 \tag{26}$$

$$D_U(\boldsymbol{\Phi}) = \frac{1}{2} \sum_{k=1}^{N_{\text{meas}}} \{U(\boldsymbol{\Phi})[k] - y_U[k]\}^2. \tag{27}$$

Then define

$$D_{\text{Stokes}}(\boldsymbol{\Phi}) = D_{\text{radiance}}(\boldsymbol{\Phi}) + D_Q(\boldsymbol{\Phi}) + D_U(\boldsymbol{\Phi}). \tag{28}$$

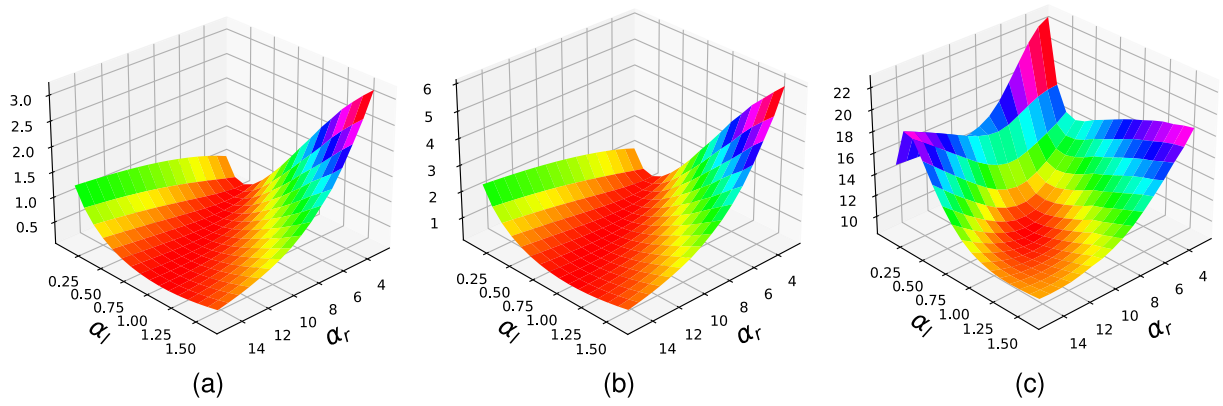

Fig. 12. (a) D_{radiance}, (b) D_{Stokes}, and (c) D_{DoLP} as a function of initialization parameters.

TABLE I
SUMMARY OF INITIALIZATION METHODS

Method	Model	Initialization parameters	Method of setting the two parameters	Cost function
$\text{H}_{\text{Typical}}$	Homogeneous	$\mathbf{\Phi} = [\text{LWC}_0, r_{\text{e}0}]$	Typical values $\mathbf{\Phi} = \left[\text{LWC}_0 = 0.01\,[\frac{\text{g}}{\text{m}^3}], r_{\text{e}0} = 12\,[\mu\text{m}]\right]$	
H_{Stokes}	Homogeneous	$\mathbf{\Phi} = [\text{LWC}_0, r_{\text{e}0}]$	Cost function minimization	D_{Stokes}
M_{Stokes}	Monotonous	$\mathbf{\Phi} = [\alpha_{\text{l}}, \alpha_{\text{r}}]$	Cost function minimization	D_{Stokes}
M_{DoLP}	Monotonous	$\mathbf{\Phi} = [\alpha_{\text{l}}, \alpha_{\text{r}}]$	Cost function minimization	D_{DoLP}

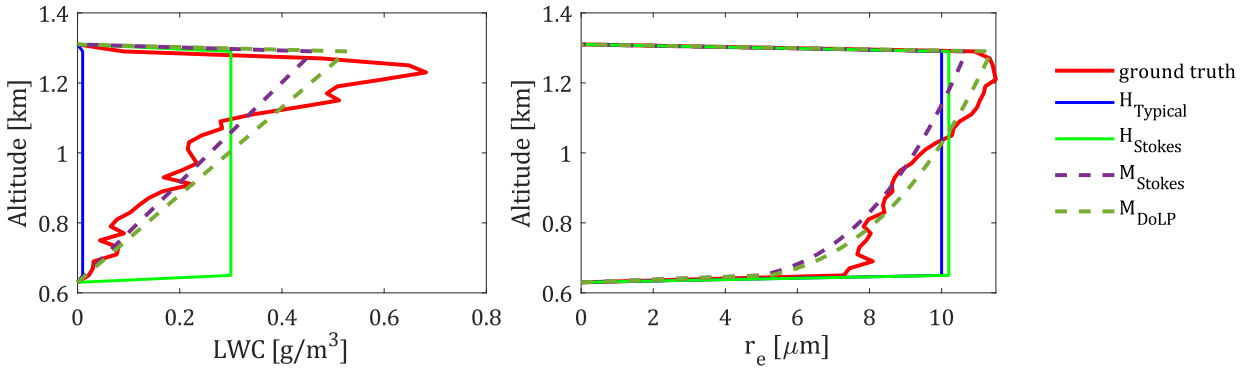

Fig. 13. Initial profiles of **LWC** and $\boldsymbol{r}_e$ for a sample cloud, as set by different initialization methods. In this cloud, the values of mean r_e and maximum OD at wavelength of 645 nm are 10 μm and 24, respectively.

Define an initialization method H_{Stokes}, which uses a homogeneous model. The parameters $\mathbf{\Phi} = [\text{LWC}_0, r_{e0}]$ are set by

$$\hat{\mathbf{\Phi}} = \arg\min_{\mathbf{\Phi}} [D_{\text{Stokes}}(\mathbf{\Phi})]. \tag{29}$$

Define an initialization method M_{Stokes}, which uses a monotonous model: the parameters $\mathbf{\Phi} = [\alpha_l, \alpha_r]$ are set after minimization as in (29).

A different considered cost is defined by the difference between the modeled DoLP$[k](\mathbf{\Phi})$ and the measured DoLP, denoted $y_{\text{DoLP}}[k]$

$$D_{\text{DoLP}}(\mathbf{\Phi}) = \frac{1}{2}\sum_{k=1}^{N_{\text{meas}}} \{\text{DoLP}(\mathbf{\Phi})[k] - y_{\text{DoLP}}[k]\}^2. \tag{30}$$

An initialization denoted M_{DoLP} which uses a monotonous model sets the initialization parameters $\mathbf{\Phi} = [\alpha_l, \alpha_r]$ by

$$\hat{\mathbf{\Phi}} = \arg\min_{\mathbf{\Phi}} [D_{\text{DoLP}}(\mathbf{\Phi})]. \tag{31}$$

Examples of the cost for a particular cloud, using the monotonous model, are presented in Fig. 12. The cost D_{DoLP} has a better-defined minimum. This example indicates that there is a potential advantage to use the DoLP for setting $\mathbf{\Phi}$. The different methods are summarized in Table I. An example of initialization profiles of **LWC** and $\boldsymbol{r}_e$ is plotted in Fig. 13.

V. PRECONDITIONING AND ALTERNATING OPTIMIZATION

This section relates to Stage 3: high-dimensional optimization of CT (see Section II-B, and Fig. 1). The optimization attempts to solve a problem, which consists of unknowns whose commonly used numerical scale differs by orders

of magnitude. In small clouds (up to a domain of $1 \times 1 \times 1$ km^3), typical maximum values of LWC and r_e are 1 (g/m^3), and 15 μm, respectively. An optimization based on gradient descent can be highly affected by this relative scale.

One way to overcome this effect is a preconditioning of the scales of the variables, which sets them at the same order of magnitude, as done by Levis *et al.* [18]. They define preconditioning factors of $\Pi_{\text{LWC}} = 15$ and $\Pi_{r_e} = 0.01$, which multiply the gradients of $\widehat{\mathbf{LWC}}$ and $\widehat{\boldsymbol{r}_e}$, respectively.

However, we find that the preconditioning is cloud-sensitive. Levis *et al.* [18] assume a 1-D structure of $\boldsymbol{r}_e$ retrieval. For $\boldsymbol{r}_e$ with 3-D spatial variation, we find preconditioning factors of $\Pi_{\text{LWC}} = 10$ and $\Pi_{r_e} = 0.1$ to be useful.

We also consider a different approach that requires no preconditioning: Alternating optimization rounds of either a **LWC** optimization round or an $\boldsymbol{r}_e$ optimization round, exclusively.

VI. Simulations

Data acquisition is currently simulated and the inverse methods are applied on this simulation. This section is divided into three parts. Section VI-A describes the simulation settings. Then inversion results are shown in Section VI-B. Possible errors are discussed in Section VI-C.

A. Settings

We simulate the satellites and Sun in the TE coordinate system. The orbit of the satellites and their positions are set as described in Appendix I. The satellites move in the positive direction of $\hat{\boldsymbol{X}}$, while $\hat{\boldsymbol{Y}} = 0$. Let θ_{sat} and ϕ_{sat} be the zenith and azimuth angles of the satellite, respectively (see Fig. 2). For simplicity, we set ϕ_{sat} to zero (Appendix I). Each imager aims to the center of the cloud field. In practice, the satellites have an inevitable pointing error. Still, part of the cloud field is viewed by all satellites simultaneously. To demonstrate the concept of this article, we focus only on this FOV part, which is viewed simultaneously from all the satellites. Let θ_{sun} and ϕ_{sun} be the zenith and azimuth angles of the Sun (see Fig. 2). In the current demonstration, $\theta_{\text{sun}} = 25°$ and $\phi_{\text{sun}} = 90°$.

Cloud properties within the field are defined according to LES [59], based on the Barbados oceanographic and meteorology experiment (BOMEX) [60]. The LES results are precomputed and serve as ground-truth, including microphysics of the cloud. The voxel size is $20 \times 20 \times 20$ m^3. RT through these 3-D fields is modeled by pySHDOM as in [13], [14], [18], [61]. We used a set of six clouds having characteristics as summed in Table II.

An image formation model of a polarized camera is used to generate the multiview images, including radiometric noise (see Appendix III). To achieve the conclusions of this study, we save computation time, by studying a camera of about 1×1 km^2 FOV. The FOV is tuned to acquire a cloud of interest from the LES. We then set the FOV as centered at the $(0, 0, 0)$ coordinates in the TE system.

B. Tomography Results

In the reconstruction, the effective variance υ_e is assumed constant, $\upsilon_e = 0.1$. The retrieval assumes a ground-truth 3-D mask, which is extracted from the 3-D extinction field of the cloud data.

TABLE II
Summary of Ground-Truth Characteristics of a Cloud-Set Used in Our Simulations

Maximum r_{e} [μm]	8.8 - 15.4
Mean r_{e} [μm]	6.2 - 10
Maximum cloud optical-depth	19.2 - 71.8
Minimum cloud base altitude [m]	550
Maximum cloud top altitude [m]	1710

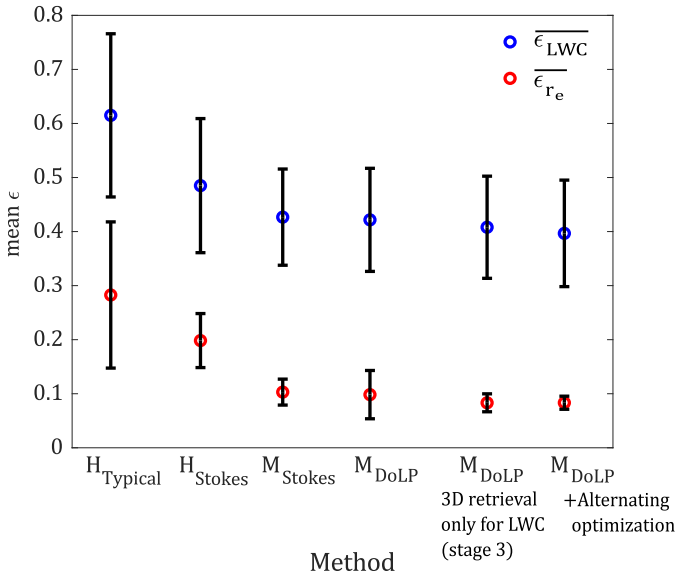

Fig. 14. Summary of mean error values following Stage 3, following different initializations set in Stage 2. Bars represent the standard deviation of errors.

For each initialization method, $\overline{\epsilon_{\mathbf{LWC}}}$ and $\overline{\epsilon_{r_e}}$ are estimated (see 7, 8). A comparison (presented in Fig. 14) demonstrates the superiority of M_{Stokes} and M_{DoLP} for initialization. These methods use the monotonous cloud model (see 23, 24).

The difference in errors of M_{Stokes} and M_{DoLP} is very small, with a slight advantage to M_{DoLP}. For some of the clouds sampled, these two methods result in the same parameters for initialization of Stage 3. For the few clouds that yielded significantly different parameters, we find an improvement in favor of M_{DoLP}. For this reason, it appears there is a benefit to use M_{DoLP} for initialization. The advantage of M_{DoLP} is in clouds having (vertical) optical-depth values below 30. In a scattering medium, a lower optical-depth corresponds to less multiple scattering. This is equivalent to a higher weight of single scattering, in which polarization is significant. The scientific goals of the CloudCT mission are focused on small warm clouds. Therefore, it is a reasonable assumption that a significant part of the actual data acquired in the mission has the order of these low optical-depth values.

We find that the 1-D model assumed for $\boldsymbol{r}_e$ (see 24) proves to be a good assumption. As demonstrated in Fig. 14, Stage 2 (see Section IV, and Fig. 1) may suffice for estimation of $\boldsymbol{r}_e$. Here, $\boldsymbol{r}_e$ and **LWC** are set by the M_{DoLP} initialization

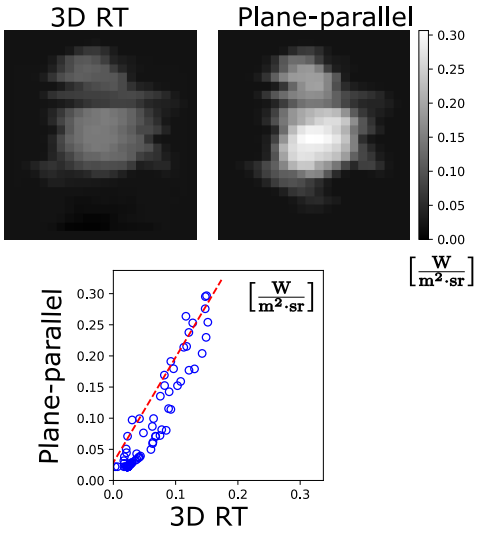

Fig. 15. (Left) Rendered cloud images based on 3-D RT. (Right) Plane parallel assumption. The pixel values of the approaches are compared via a scatter plot.

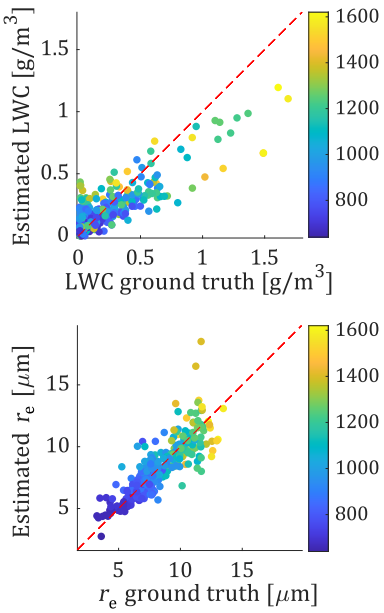

Fig. 16. Scatter plots of retrievals sampled from the whole cloud-set. The color bar represents the altitude of the sample.

method (Stage 2). Afterward, only the **LWC** is retrieved in 3-D (Stage 3). The 3-D CT problem is thus mainly that of estimating the **LWC** in 3-D, while $\boldsymbol{r}_e$ is approximated by a 1-D function, as in prior research [18], [23], [38].

Alternating optimization removes the need for preconditioning of the scales of the variables, and thus removes a complication from the optimization. In addition, we find that alternating optimization (Section V) yields an additional retrieval improvement (see Fig. 14, here the M_{DoLP} initialization method is assumed). However, alternating optimization increases the run-time significantly.

C. Discussion of Errors

Errors of a plane-parallel model arise from neglecting lateral effects of RT. These effects increase with the solar zenith angle. A quantitative comparison of rendered cloud images based on 3-D RT and plane-parallel assumption is presented in Fig. 15. This rendering is an orthographic projection of a 3-D cloud scene.[4] In plane-parallel rendering, each pixel is fit to a specific 1-D column, effectively following the IPA [31]. In IPA, each pixel is isolated from its neighbors, i.e., there are no radiative interactions between vertical columns underlying neighboring pixels. The wavelength in this demonstration is 652 nm, and $\theta_{\text{sun}} = 25°$. Fig. 15 illustrates that a small cloud rendered by an IPA approach is brighter than that of 3-D RT rendering, since the horizontal fluxes are treated differently. Higher reflectance in an image based on the IPA would cause overestimation in $\boldsymbol{r}_e$ retrieval [5]. In contrast, the 3-D RT model includes lateral RT. So, 3-D RT reduces this overestimation.[5]

In the current simulation, retrieval errors stem from physical and optical constraints and algorithmic capacities. As Forster *et al.* [26] demonstrate, a veiled core of a cloud limits tomography. We will continue to explore the error in clouds of focus in CloudCT.

Retrieval accuracy depends also on the signal-to-noise (SNR) ratio. A thorough analysis of the effects of electronic noise, airlight, and stray light on the SNR will be discussed in our future work.

In algorithmic aspects, as demonstrated, retrieval highly depends on initialization. In addition, there is uncertainty stemming from the process of space carving. In space-carving, image processing and stereo imaging are used to set a domain of interest. However, the cloud base is not directly viewed by spaceborne imagers. So, there may be a higher uncertainty of the cloud geometry there.

An additional biasing effect can be seen in the retrieval of the **LWC**. This can be seen in the scatter plots presented in Fig. 16. Here, a tendency of underestimation of LWC is apparent. These errors will be further examined. We believe that algorithmic advances will counter this error.

VII. Conclusion

We introduce a comprehensive method for spaceborne 3-D volumetric scattering-tomography of cloud microphysics. The method is tailored for the CloudCT space mission, of 3-D scattering tomography of warm clouds. It includes adjustments to the pySHDOM 3-D microphysical scattering tomography. The major adjustments are implementation of a realistic polarized imager model, and a new initialization method. We demonstrate the superiority of an initialization method based on a parameterized horizontally uniform model, under the constraints of the implemented imager model. For small clouds with low values of vertical OD, we find that initialization based on the DoLP has an advantage. For the CloudCT

[4]This orthographic projection is not used in the inversion.

[5]A plane parallel atmosphere assumption also neglects the curved geometry of the atmosphere. For retrieval of clouds in a wide medium, this is significant. However, in the scale of the medium that we examine, this effect is negligible.

mission which focuses on small clouds, this may be significant. In addition, we suggest cloudbow scanning.

Future research toward the CloudCT mission will further address the potential of the cloudbow-scan. The final orbit plan will be taken into consideration, along with a statistical analysis of the satellite pointing accuracy, maneuver capabilities, and payload frame rate.

Following our conclusion regarding the advantage of the DoLP error to initialization, we have begun an initial examination of the possibility of full optimization (Stage 3) based on the DoLP error. Currently, this has not proven useful. This may be due to the low values of DoLP outside of the cloudbow. However, future research may examine other cost function formats, which consider errors of different combinations of the Stokes vector components.

The proposed method has not been tested on large precipitating clouds such as Cumulonimbus. In such clouds, there is a mixed phase. That is, the cloud is made of ice crystals, cloud-droplets as well as rain-drops. Such clouds appear also in extreme weather conditions. These are not the focus of CloudCT. Ice crystals have different optical properties. Moreover, rain-drops are much larger than cloud droplets. Further research may include the phase functions of ice particle and rain drops. SHDOM can express RT by ice crystals of eight specific shapes [62], based on [63], assuming no preferred orientation. However, this is currently not implemented in pySHDOM. In addition, heavy precipitation and severe convection may cause rapid changes in liquid water content. Here, simultaneity of multiangular imaging would be an advantage to sequential imaging as in MISR, AirMSPI and POLDER. Regardless of the polarized sensing approach, we believe that our scattering tomography approach can be relevant in additional tomographic setups, for instance, in the mesospheric airglow/aerosol tomography and spectroscopy (MATS) [64].

Appendix I
Earth Coordinate System

Here, we describe the coordinates of the satellites. For simplicity, let the Earth be a sphere having radius $R_{\text{earth}} = 6371$ km. We used the EC and TE coordinate systems (see Section III-A). Both are illustrated in Fig. 3.

Let ξ_{sat} be the zenith angle of the satellite, in the EC coordinate system (Fig. 3). Let L be the distance (on the orbit arc) between two adjacent satellites ($L = 100$ km as described in Section III-B). The angular distance between two adjacent satellites is

$$\Delta\xi_{\text{sat}} = \frac{L}{R_{\text{earth}} + R_{\text{orbit}}}. \tag{32}$$

Let $j \in [1, 10]$ be an index of a satellite. Satellite angles $\{\xi_{\text{sat}}[j]\}_{j=1}^{10}$ are equally spread. The satellite location in the EC coordinate system is

$$\begin{aligned} X_{\text{earth}}[j] &= (R_{\text{earth}} + R_{\text{orbit}})\sin(\xi_{\text{sat}}[j]) \\ Y_{\text{earth}}[j] &= 0 \\ Z_{\text{earth}}[j] &= (R_{\text{earth}} + R_{\text{orbit}})\cos(\xi_{\text{sat}}[j]). \end{aligned} \tag{33}$$

So, in the EC coordinate system

$$\xi_{\text{sat}}[j] = \tan^{-1}\left(\frac{X_{\text{earth}}[j]}{Z_{\text{earth}}[j]}\right) = \cos^{-1}\left(\frac{Z_{\text{earth}}[j]}{R_{\text{earth}} + R_{\text{orbit}}}\right). \tag{34}$$

In the TE coordinate system, the satellite coordinates are

$$\begin{aligned} X[j] &= X_{\text{earth}}[j] \\ Y[j] &= 0 \\ Z[j] &= Z_{\text{earth}}[j] - R_{\text{earth}}. \end{aligned} \tag{35}$$

In TE Earth system (Fig. 3), the zenith angle of the satellite is

$$\theta_{\text{sat}}[j] = \tan^{-1}\left(\frac{X[j]}{Z[j]}\right). \tag{36}$$

Appendix II
Cloudbow-Scan Time-Scale

Here, we show that the time-scale for the cloudbow-scan may reach ≈30 s. As demonstrated in [51], this is an acceptable time scale regarding cloud development. In the simulations presented in this article, the range of the scanned scattering angles in the cloudbow is $135^\circ \le \theta_{\text{sca}} \le 150^\circ$. We uniformly sample ten angles in this range.

Using the same convention as described in Figs. 2 and 3 ($\phi_{\text{sat}} = 0^\circ$), the direction vector from the Sun to the domain is

$$\hat{\mathbf{d}}_{\text{sun}} = \begin{bmatrix} \sin(180 - \theta_{\text{sun}})\cos(\phi_{\text{sun}}) \\ \sin(180 - \theta_{\text{sun}})\sin(\phi_{\text{sun}}) \\ \cos(180 - \theta_{\text{sun}}) \end{bmatrix}. \tag{37}$$

The direction from the origin of the TE coordinate system to the satellite is

$$\hat{\mathbf{d}}_{\text{sat}} = \begin{bmatrix} \sin(\theta_{\text{sat}}) \\ 0 \\ \cos(\theta_{\text{sat}}) \end{bmatrix}. \tag{38}$$

Only at the central pixel, $\hat{\mathbf{d}}_{\text{sat}} = \boldsymbol{\omega}$. The scattering angle θ_{sca} (see Fig. 8) is calculated by

$$\theta_{\text{sca}} = \cos^{-1}(\hat{\mathbf{d}}_{\text{sat}} \cdot \hat{\mathbf{d}}_{\text{sun}}) \tag{39}$$

which yields

$$\theta_{\text{sca}} = \cos^{-1}[\sin(\theta_{\text{sat}})\sin(\theta_{\text{sun}})\cos(\phi_{\text{sun}}) + \cos(\theta_{\text{sat}})\cos(\theta_{\text{sun}})]. \tag{40}$$

The angles ξ_{sat} and θ_{sat} (and generally, the azimuth angles ϕ_{sat}) can be set to a specific angular range relative to $\hat{\mathbf{d}}_{\text{sun}}$, specifically within the cloudbow. This requires inverting (40), and extracting θ_{sat} as a function of θ_{sca}. We solve this numerically. First, angle samples ξ_{sat} are converted to angle samples θ_{sat} (using 33, 35 and 36). Then, by numerical search of (40), we seek samples θ_{sat} that provide the required samples of θ_{sca}.

Let ξ'_{sat} be a zenith angle of the satellite, in the EC coordinate system, sampled at much higher resolution than ξ_{sat} (Fig. 17). The goal of using angles ξ'_{sat} is to discretize the position on the orbit path with high resolution. We generate 1310 samples of $\xi'_{\text{sat}} \in [\xi_{\text{sat}}[1], \xi_{\text{sat}}[10]]$. Let q be an index of ξ'_{sat}. For each sample $\{\xi'_{\text{sat}}[q]\}_{q=1}^{1310}$, we calculate a sample $\{\theta'_{\text{sat}}[q]\}_{q=1}^{1310}$, using (33, 35) and (36). Let e be an index of the

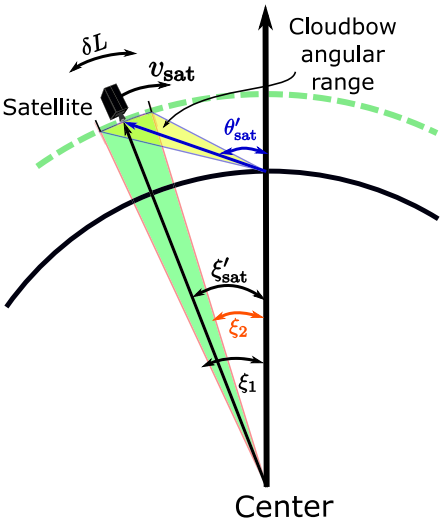

Fig. 17. Satellite's zenith angles ξ'_{sat} and θ'_{sat} that are used to sample the orbit, to meet the cloudbow-scan goal.

scattering angle θ_{sca}. For each of the ten samples $\{\theta_{sca}[e]\}_{e=1}^{10}$, we find the index q which best satisfies (40), that is

$$\hat{q} = \arg\min_{q} \mid \Omega[q, e] \mid \tag{41}$$

where

$$\Omega[q, e] = \theta_{sca}[e] - \cos^{-1}[\sin(\theta_{sat}[q])\sin(\theta_{sun})\cos(\phi_{sun}) + \cos(\theta_{sat}[q])\cos(\theta_{sun})]. \tag{42}$$

Finally, the respective angle $\xi'_{sat}[\hat{q}]$ is extracted. The angle $\xi'_{sat}[\hat{q}]$ is the zenith angle of a satellite that observes the cloudbow angular range, in the EC coordinate system. Given ten such angles, we extract the two extreme and denote them by ξ_1 and ξ_2 (Fig. 17). These two extreme angles are used to assess the time that is needed to scan the cloudbow by one satellite.

Let v_{sat} be the velocity of the satellite (Fig. 17). For orbit radius $(R_{earth} + R_{orbit})$, the velocity is

$$v_{sat} = \sqrt{\frac{\mu_g}{R_{earth} + R_{orbit}}} \tag{43}$$

where [65] $\mu_g = 3.986004418 \cdot 10^5$ (km^3/s^2) is the standard gravitational parameter. In a low-Earth orbit, $v_{sat} \approx 7.6$ (km/s). The distance that a satellite travels (Fig. 17) on the orbital arc between the two angles ξ_1 and ξ_2 is

$$\delta L = \|\xi_1 - \xi_2\|(R_{earth} + R_{orbit}). \tag{44}$$

The time T in which the satellite scans the cloudbow angular region is

$$T = \frac{\delta L}{v_{sat}}. \tag{45}$$

As an example, consider satellite 9 in the setup described in Section III-B (see Fig. 6). Let it capture ten samples in the cloudbow angular range [135°,150°]. Then, the total cloudbow-scan time is ≈31.23 s. For a $\hat{\mathbf{d}}_{sat}$ and $\hat{\mathbf{d}}_{sun}$ where a cloudbow-scan satellite is nadir observing (as in Fig. 8), faster frame rates are required. In such a configuration, the scan time is ≈20 s.

Appendix III
Imager Model

As in [18], we use an image formation model for both the forward and inverse models. Let us denote spectral band by Λ. There, the wavelength λ is between $[\lambda_1, \lambda_2]$. Let us denote spectral radiance at wavelength λ by I_λ. It is calculated by pySHDOM and has units of (W/m$^2 \cdot$ sr $\cdot$ nm). The camera yields *perspective projection*. The perspective projection is implemented in pySHDOM.

The camera system efficiency due to optical losses at wavelength λ is τ_λ. Consider a camera with a lens of diameter D at distance f from the focal plane. Lens distortions are assumed to be known and compensated for. The camera is focused on the object (i.e., clouds). For simplicity assume I_λ is uniform within the area of a pixel footprint on the cloud. Geometrically, this is equivalent to uniform irradiance on the detector pixel (area p^2). We consider the pixels to be close to the optical axis of the camera.[6]

To simulate a readout of the imager, we convert I_λ within Λ to photo-generated electrons in the sensor, as follows.[7] Light energy is converted to the expected number of photons at wavelength λ by the factor $(\lambda/\mathtt{h}\,\mathtt{c})$ (photons/Joule). A pixel on a sensor responds to the photons in a spectral band Λ. The pixel response depends on the sensor's quantum efficiency, QE_λ (electrons/photons). It is a measure of the probability for a photo-electron to be created per incident photon with wavelength λ.

Let Δt be the exposure time of the imager. The expected number of photo-electrons that are created in a pixel is

$$N_\Lambda = p^2 \Delta t \int_\Lambda \tau_\lambda \mathrm{QE}_\lambda \frac{\lambda}{\mathtt{h}\,\mathtt{c}} \pi \left(\frac{D}{2f}\right)^2 I_\lambda d\lambda = \Delta t \int_\Lambda \Gamma_\lambda I_\lambda d\lambda \quad \text{electrons}. \tag{46}$$

Here, we define

$$\Gamma_\lambda = \pi \tau_\lambda \left(\frac{D}{2f}\right)^2 \mathrm{QE}_\lambda \frac{\lambda}{\mathtt{h}\,\mathtt{c}} p^2 \quad \frac{\text{electrons} \cdot \text{m}^2 \cdot \text{sr}}{\text{Joule}} \tag{47}$$

which encapsulates dependencies on the optics, pixel size, QE, and the pixel's receptive solid-angle.

Ideally, to calculate the integral in (46), RT would be run multiple times to calculate I_λ in the spectral band Λ, at a high wavelength resolution. There is a common approximation that simplifies these calculations [13], [61]. Instead of multiple calculations of I_λ within Λ, in this approximation, RT is simulated only once. Let $\tilde{I}_\lambda$ be the spectral radiance which is a result of this single RT run i.e., $\tilde{I}_\lambda$ is an approximation of I_λ. The field $\tilde{I}_\lambda$ is used instead of I_λ in (46), and has the same units as I_λ. When Γ_λ is significant, the approximation $\tilde{I}_\lambda \approx I_\lambda$ is valid if wavelength dependencies within a spectral band are weak. This condition is met when narrow bands are considered (e.g., up to 40 nm [13]). Under these assumptions, the optical

[6] Away from the optical axis, there is often vignetting, which refers to radial fall-off of pixel intensity from the camera's optical axis toward the edges of the image [66], [67]. For narrow FOV imagers, as we deal with, vignetting is considered manageable.

[7] For a sensor having a linear radiometric response, the conversion between electrons and the sensor readout value in gray-scale is by a fixed ratio. We do not deal with gray-scale values in this article.

quantities can be spectrally averaged over Λ. Then spectrally averaged optical quantities are used as constants within Λ.

Next, we describe how to express $\tilde{I}_\lambda$. Let I_Λ be the spectral radiance output of pySHDOM if the top of the atmosphere (TOA) is irradiated by $1(\mathrm{W/m^2 \cdot nm})$. Since the optical quantities are spectrally averaged within Λ, I_Λ is fixed within Λ. The units of I_Λ are $(\mathrm{W/m^2 \cdot sr \cdot nm})$. Let $\Upsilon_\lambda^{\mathrm{TOA}}$ be a unitless function of λ. This function scales the TOA irradiance of $1(\mathrm{W/m^2 \cdot nm})$ to the true solar irradiance at the TOA. The spectral radiance $\tilde{I}_\lambda$ is the radiance simulated by RT, if the TOA irradiance is $\Upsilon_\lambda^{\mathrm{TOA}} \cdot 1(\mathrm{W/m^2 \cdot nm})$. Therefor

$$\tilde{I}_\lambda = I_\Lambda \Upsilon_\lambda^{\mathrm{TOA}} \frac{\mathrm{W}}{\mathrm{m^2 \cdot sr \cdot nm}}. \tag{48}$$

As $\tilde{I}_\lambda \approx I_\lambda$, (46) becomes

$$N_\Lambda = \Delta t I_\Lambda \int_\Lambda \Gamma_\lambda \Upsilon_\lambda^{\mathrm{TOA}} d\lambda \quad \text{electrons}. \tag{49}$$

From (49), a conversion factor A_Λ converts a photo-electron count to radiance

$$A_\Lambda = \frac{1}{\Delta t \int_\Lambda \Gamma_\lambda \Upsilon_\lambda^{\mathrm{TOA}} d\lambda} \quad \frac{\mathrm{W}}{\mathrm{electrons \cdot m^2 \cdot sr}}. \tag{50}$$

To simulate raw measurements, we introduce noise to N_Λ. First, we incorporate *photon shot noise*, which is Poisson-distributed around the expected value N_Λ. The resulting photo-electron value $\tilde{N_\Lambda}$ is

$$\tilde{N_\Lambda} \sim \mathrm{Poisson}\{N_\Lambda\} \quad \text{electrons}. \tag{51}$$

Then, we introduce more noise sources according to the sensor specifications. We simulate the readout noise, dark current shot noise, and quantization noise.

Let $\mathcal{N}(\mathrm{mean}, \mathrm{STD})$ be a normal distribution with standard deviation STD. Let operator $\lfloor \cdot \rfloor$ be a floor function. The readout noise has a standard deviation of $\mathrm{STD_{read}}$ electrons. We simulate the readout random noise contribution in electrons units by $\lfloor \mathcal{N}(0, \mathrm{STD_{read}}) \rfloor$. The dark current shot noise at temperature τ is $\mathcal{B}_\tau$ (electrons/second). The dark current shot noise is Poisson-distributed. We simulate the dark current shot random noise contribution in electrons units by $\lfloor \mathcal{N}\left(\mathcal{B}_\tau \Delta t, \sqrt{\mathcal{B}_\tau \Delta t}\right) \rfloor$. Quantization noise is introduced by simply scaling the electrons to gray-scale levels, then applying a floor operator, and finally scaling back. The maximum number of electrons which can be contained in a pixel is the *full well* capacity.[8] Pixel readout is quantized by *bits*, i.e., pixel values in gray-scale can be in the range of $[0, 2^{\mathrm{bits}}]$. We simulate measured photo-electrons by

$$N_\Lambda^{\mathrm{measured}} = \frac{\text{full well}}{2^{\mathrm{bits}}} \left\lfloor \frac{2^{\mathrm{bits}}}{\text{full well}} \left[\tilde{N_\Lambda} + \lfloor \mathcal{N}(0, \mathrm{STD_{read}}) \rfloor - \left\lfloor \mathcal{N}(\mathcal{B}_\tau \Delta t, \sqrt{\mathcal{B}_\tau \Delta t}) \right\rfloor \right] \right\rfloor \quad \text{electrons}. \tag{52}$$

The value $N_\Lambda^{\mathrm{measured}}$ is clipped to the range [0, full well].

In our simulations, the exposure time Δt is set to a level such that the sensor reaches 90% of its full well. Noise specifications in our simulation are based on Sony's IMX250MYR sensor [48]. The pixel size is $3.45 \times 3.45\ \mu\mathrm{m}^2$, $\mathrm{STD_{read}} = 2.31$ electrons, $\mathcal{B}_\tau = 3.51$(electrons/second) at 25 °C. The full-well is 10 500 electrons. We use 10-bit quantization.

To convert the measured photo-electron count $N_\Lambda^{\mathrm{measured}}$ to measured radiance $I_\Lambda^{\mathrm{measured}}$, we use (49) and (50)

$$I_\Lambda^{\mathrm{measured}} = A_\Lambda N_\Lambda^{\mathrm{measured}} \quad \frac{\mathrm{W}}{\mathrm{m^2 \cdot sr}}. \tag{53}$$

[8]Sensor suppliers specify the full well in units of electrons.

ACKNOWLEDGMENT

The authors are grateful to Orit Altaratz, Anthony Davis, and Linda Forster for useful discussions and good advice. The authors would like to thank Aviad Levis and Jesse Loveridge for the pySHDOM code, for useful discussions and being responsive to questions about it. The authors would also like to thank Miri Haramati, Johanan Erez, Ina Talmon, and Daniel Yagodin for technical support. Yoav Schechner is the Mark and Diane Seiden Chair in science at the Technion. He is a Landau Fellow–supported by the Taub Foundation. His work was conducted in the Ollendorff Minerva Center. Minvera is funded through the BMBF.

REFERENCES

[1] *CloudCT Spaceborne Cloud Tomography*. [Online]. Available: https://www.cloudct.space/

[2] A. Davis, A. Marshak, R. Cahalan, and W. Wiscombe, "The landsat scale break in stratocumulus as a three-dimensional radiative transfer effect: Implications for cloud remote sensing," *J. Atmos. Sci.*, vol. 54, no. 2, pp. 241–260, Jan. 1997.

[3] T. Várnai and A. Marshak, "Statistical analysis of the uncertainties in cloud optical depth retrievals caused by three-dimensional radiative effects," *J. Atmos. Sci.*, vol. 58, no. 12, pp. 1540–1548, Jun. 2001.

[4] T. Zinner and B. Mayer, "Remote sensing of stratocumulus clouds: Uncertainties and biases due to inhomogeneity," *J. Geophys. Res.*, vol. 111, no. D14, 2006, Art. no. D14209.

[5] A. Marshak, S. Platnick, T. Várnai, G. Wen, and R. F. Cahalan, "Impact of three-dimensional radiative effects on satellite retrievals of cloud droplet sizes," *J. Geophys. Res.*, vol. 111, no. D9, 2006, Art. no. D09207.

[6] C. Matar, C. Cornet, F. Parol, L. C-Labonnote, F. Auriol, and J.-M. Nicolas, "Cloud optical properties retrieval and associated uncertainties using multi-angular and multi-spectral measurements of the airborne radiometer osiris," *Atmos. Meas. Techn. Discuss.*, 2022. [Online]. Available: https://amt.copernicus.org/preprints/amt-2021-414/, doi: 10.5194/amt-2021-414.

[7] D. Fu *et al.*, "An evaluation of liquid cloud droplet effective radius derived from MODIS, airborne remote sensing and *in situ* measurements from CAMP2Ex," *Atmos. Chem. Phys. Discuss.*, vol. 22, no. 12, pp. 8259–8285, Jun. 2022. [Online]. Available: https://acp.copernicus.org/articles/22/8259/2022/acp-22-8259-2022.html, doi: 10.5194/acp-22-8259-2022.

[8] C. Cornet, L. C-Labonnote, and F. Szczap, "Three-dimensional polarized Monte Carlo atmospheric radiative transfer model (3DMCPOL): 3D effects on polarized visible reflectances of a cirrus cloud," *J. Quant. Spectrosc. Radiat. Transf.*, vol. 111, no. 1, pp. 174–186, Jan. 2010.

[9] R. Marchand, "Evaluation of radiometric measurements from the NASA multiangle imaging spectroradiometer (MISR): Two- and three-dimensional radiative transfer modeling of an inhomogeneous stratocumulus cloud deck," *J. Geophys. Res.*, vol. 109, no. D18, 2004.

[10] A. Marshak and A. Davis, *3D Radiative Transfer in Cloudy Atmospheres*. Cham, Switzerland: Springer, 2005.

[11] B. Mayer, "Radiative transfer in the cloudy atmosphere," *Eur. Phys. J.-Special Topics*, vol. 1, pp. 75–99, Feb. 2009.

[12] A. Levis, Y. Y. Schechner, A. Aides, and A. B. Davis, "Airborne three-dimensional cloud tomography," in *Proc. IEEE Int. Conf. Comput. Vis. (ICCV)*, Dec. 2015, pp. 3379–3387.

[13] A. Levis, Y. Y. Schechner, and A. B. Davis, "Multiple-scattering microphysics tomography," in *Proc. IEEE Conf. Comput. Vis. Pattern Recognit. (CVPR)*, Jul. 2017, pp. 6740–6749.

[14] Y. Sde-Chen, Y. Y. Schechner, V. Holodovsky, and E. Eytan, "3DeepCT: Learning volumetric scattering tomography of clouds," in *Proc. IEEE/CVF Int. Conf. Comput. Vis. (ICCV)*, Oct. 2021, pp. 5671–5682.

[15] K. F. Evans, "The spherical harmonics discrete ordinate method for three-dimensional atmospheric radiative transfer," *J. Atmos. Sci.*, vol. 55, no. 55, pp. 429–446, Feb. 1998.

[16] A. Levis, J. Loveridge, and A. Aides. (2019). *pySHDOM*. [Online]. Available: https://github.com/aviadlevis/pyshdom

[17] A. Doicu, D. Efremenko, and T. Trautmann, "A multi-dimensional vector spherical harmonics discrete ordinate method for atmospheric radiative transfer," *J. Quant. Spectrosc. Radiat. Transf.*, vol. 118, pp. 121–131, Mar. 2013, doi: 10.1016/j.jqsrt.2012.12.009.

[18] A. Levis, Y. Y. Schechner, A. B. Davis, and J. Loveridge, "Multi-view polarimetric scattering cloud tomography and retrieval of droplet size," *Remote Sens.*, vol. 12, no. 17, p. 2831, Sep. 2020.

[19] F.-M. Bréon and P. Goloub, "Cloud droplet effective radius from spaceborne polarization measurements," *Geophys. Res. Lett.*, vol. 25, no. 11, pp. 1879–1882, Jun. 1998.

[20] F. Parol *et al.*, "Review of capabilities of multi-angle and polarization cloud measurements from POLDER," *Adv. Space Res.*, vol. 33, no. 7, pp. 1080–1088, Jan. 2004.

[21] F. M. Breon and M. Doutriaux-Boucher, "A comparison of cloud droplet radii measured from space," *IEEE Trans. Geosci. Remote Sens.*, vol. 43, no. 8, pp. 1796–1805, Aug. 2005.

[22] N. J. Pust and J. A. Shaw, "Wavelength dependence of the degree of polarization in cloud-free skies: Simulations of real environments," *Opt. Exp.*, vol. 20, no. 14, pp. 15559–15568, Jul. 2012. [Online]. Available: http://www.opticsexpress.org/abstract.cfm?URI=oe-20-14-15559

[23] M. D. Alexandrov, B. Cairns, C. Emde, A. S. Ackerman, and B. van Diedenhoven, "Accuracy assessments of cloud droplet size retrievals from polarized reflectance measurements by the research scanning polarimeter," *Remote Sens. Environ.*, vol. 125, pp. 92–111, Oct. 2012, doi: 10.1016/j.rse.2012.07.012.

[24] H. Shang *et al.*, "An improved algorithm of cloud droplet size distribution from POLDER polarized measurements," *Remote Sens. Environ.*, vol. 228, pp. 61–74, Jul. 2019, doi: 10.1016/j.rse.2019.04.013.

[25] K. Sinclair *et al.*, "Polarimetric retrievals of cloud droplet number concentrations," *Remote Sens. Environ.*, vol. 228, pp. 227–240, Jul. 2019, doi: 10.1016/j.rse.2019.04.008.

[26] L. Forster, A. B. Davis, D. J. Diner, and B. Mayer, "Toward cloud tomography from space using MISR and MODIS: Locating the 'veiled core' in opaque convective clouds," *J. Atmos. Sci.*, vol. 78, no. 1, pp. 155–166, 2021.

[27] M. Tzabari *et al.*, "CloudCT 3D volumetric tomography: Considerations for imager preference, comparing visible light, short-wave infrared, and polarized imagers," *Proc. SPIE*, vol. 11833, Aug. 2021, Art. no. 1183304.

[28] Y. Bertschy and Y. Y. Schechner, "Vicarious spaceborne polarimetric camera calibration using solar power stations," *Proc. SPIE*, vol. 12112, pp. 132–142, Jun. 2022.

[29] T. Nakajima and M. D. King, "Determination of the optical thickness and effective particle radius of clouds from reflected solar radiation measurements. Part I: Theory," *J. Atmos. Sci.*, vol. 47, no. 15, pp. 1878–1893, 1990.

[30] S. Platnick *et al.*, "The MODIS cloud optical and microphysical products: Collection 6 updates and examples from Terra and Aqua," *IEEE Trans. Geosci. Remote Sens.*, vol. 55, no. 1, pp. 502–525, Jan. 2017.

[31] A. Marshak, "The verisimilitude of the independent pixel approximation used in cloud remote sensing," *Remote Sens. Environ.*, vol. 52, no. 1, pp. 71–78, Apr. 1995.

[32] D. P. Grosvenor *et al.*, "Remote sensing of droplet number concentration in warm clouds: A review of the current state of knowledge and perspectives," *Rev. Geophys.*, vol. 56, no. 2, pp. 409–453, Jun. 2018.

[33] O. Dubovik *et al.*, "Polarimetric remote sensing of atmospheric aerosols: Instruments, methodologies, results, and perspectives," *J. Quant. Spectrosc. Radiat. Transf.*, vol. 224, pp. 474–511, Feb. 2018.

[34] B. A. McBride, J. V. Martins, H. M. J. Barbosa, W. Birmingham, and L. A. Remer, "Spatial distribution of cloud droplet size properties from airborne hyper-angular rainbow polarimeter (AirHARP) measurements," *Atmos. Meas. Techn.*, vol. 13, no. 4, pp. 1777–1796, Apr. 2020.

[35] Z. Li *et al.*, "Directional polarimetric camera (DPC): Monitoring aerosol spectral optical properties over land from satellite observation," *J. Quant. Spectrosc. Radiat. Transf.*, vol. 218, pp. 21–37, Oct. 2018.

[36] A. Di Noia, O. P. Hasekamp, B. van Diedenhoven, and Z. Zhang, "Retrieval of liquid water cloud properties from POLDER-3 measurements using a neural network ensemble approach," *Atmos. Meas. Techn.*, vol. 12, no. 3, pp. 1697–1716, Mar. 2019.

[37] J. V. Martins *et al.*, "Remote sensing the vertical profile of cloud droplet effective radius, thermodynamic phase, and temperature," *Atmos. Chem. Phys.*, vol. 11, no. 18, pp. 9485–9501, Sep. 2011.

[38] M. D. Alexandrov *et al.*, "Vertical profiles of droplet size distributions derived from cloud-side observations by the research scanning polarimeter: Tests on simulated data," *Atmos. Res.*, vol. 239, Jul. 2020, Art. no. 104924, doi: 10.1016/j.atmosres.2020.104924.

[39] K. Ebell, U. Löhnert, S. Crewell, and D. D. Turner, "On characterizing the error in a remotely sensed liquid water content profile," *Atmos. Res.*, vol. 98, no. 1, pp. 57–68, Oct. 2010.

[40] Z. Zhu, K. Lamer, P. Kollias, and E. E. Clothiaux, "The vertical structure of liquid water content in shallow clouds as retrieved from dual-wavelength radar observations," *J. Geophys. Res., Atmos.*, vol. 124, no. 24, pp. 14184–14197, Dec. 2019.

[41] D. J. Diner *et al.*, "The airborne multiangle SpectroPolarimetric imager (AirMSPI): A new tool for aerosol and cloud remote sensing," *Atmos. Meas. Techn.*, vol. 6, no. 1, pp. 2007–2025, 2013.

[42] A. Doicu, A. Doicu, D. Efremenko, and T. Trautmann, "Cloud tomographic retrieval algorithms. I: Surrogate minimization method," *J. Quant. Spectrosc. Radiat. Transf.*, vol. 277, Jan. 2022, Art. no. 107954.

[43] A. Doicu, A. Doicu, D. S. Efremenko, and T. Trautmann, "Cloud tomographic retrieval algorithms. II: Adjoint method," *J. Quant. Spectrosc. Radiat. Transf.*, vol. 285, Jul. 2022, Art. no. 108177.

[44] M. D. King *et al.*, "Cloud and aerosol properties, precipitable water, and profiles of temperature and water vapor from MODIS," *IEEE Trans. Geosci. Remote Sens.*, vol. 41, no. 2, pp. 442–458, Feb. 2003.

[45] D. J. Diner *et al.*, "Multi-angle imaging SpectroRadiometer (MISR) instrument description and experiment overview," *IEEE Trans. Geosci. Remote Sens.*, vol. 36, no. 4, pp. 1072–1087, Jul. 1998.

[46] B. Mayer, S. W. Hoch, and C. D. Whiteman, "Validating the MYSTIC three-dimensional radiative transfer model with observations from the complex topography of Arizona's meteor Crater," *Atmos. Chem. Phys.*, vol. 10, no. 18, pp. 8685–8696, Sep. 2010.

[47] R. Buras and B. Mayer, "Efficient unbiased variance reduction techniques for Monte Carlo simulations of radiative transfer in cloudy atmospheres: The solution," *J. Quant. Spectrosc. Radiat. Transf.*, vol. 112, no. 3, pp. 434–447, Feb. 2011.

[48] *Polarization Image Sensor With Four-Directional on-Chip Polarizer and Global Shutter Function*. [Online]. Available: https://www.sony-semicon.co.jp/e/products/IS/industry/product/polarization.html

[49] J. E. Hansen and L. D. Travis, "Light scattering in planetary atmospheres," *Space Sci. Rev.*, vol. 16, no. 4, pp. 527–610, 1974.

[50] S. Chandrasekhar, *Radiative Transfer*. Chelmsford, MA, USA: Courier Corporation, 2013.

[51] R. Ronen, Y. Y. Schechner, and E. Eytan, "4D cloud scattering tomography," in *Proc. ICCV*, Oct. 2021, pp. 5520–5529.

[52] L. Li, Z. Li, K. Li, L. Blarel, and M. Wendisch, "A method to calculate Stokes parameters and angle of polarization of skylight from polarized CIMEL sun/sky radiometers," *J. Quant. Spectrosc. Radiat. Transf.*, vol. 149, pp. 334–346, Dec. 2014.

[53] A. Marshak, A. Davis, W. Wiscombe, and R. Cahalan, "Radiative smoothing in fractal clouds," *J. Geophys. Res., Atmos.*, vol. 100, no. D12, pp. 26247–26261, 1995.

[54] S. Wen, Y. Zheng, and F. Lu, "A sparse representation based joint demosaicing method for single-chip polarized color sensor," 2019, *arXiv:1912.07308*.

[55] S. Mihoubi, P.-J. Lapray, and L. Bigué, "Survey of demosaicking methods for polarization filter array images," *Sensors*, vol. 18, no. 11, p. 3688, Oct. 2018.

[56] M. I. Mishchenko, L. D. Travis, and A. A. Lacis, *Scattering, Absorption, Emission Light by Small Particles*. Cambridge, U.K.: Cambridge Univ. Press, 2002.

[57] D. Veikherman, A. Aides, Y. Y. Schechner, and A. Levis, "Clouds in the cloud," in *Proc. ACCV*. Cham, Switzerland: Springer, 2014, pp. 659–674.

[58] T. Loeub, A. Levis, V. Holodovsky, and Y. Y. Schechner, "Monotonicity prior for cloud tomography," in *Proc. ECCV*. Cham, Switzerland: Springer, 2020, pp. 24–29.

[59] M. Khairoutdinov and D. Randall. (2006). *SAM*. [Online]. Available: http://rossby.msrc.sunysb.edu/~marat/SAM.html

[60] A. P. Siebesma *et al.*, "A large eddy simulation intercomparison study of shallow cumulus convection," *J. Atmos. Sci.*, vol. 60, no. 10, pp. 1201–1219, May 2003.
[61] A. Aides, A. Levis, V. Holodovsky, Y. Y. Schechner, D. Althausen, and A. Vainiger, "Distributed sky imaging radiometry and tomography," in *Proc. IEEE Int. Conf. Comput. Photography (ICCP)*, Apr. 2020, pp. 1–12.
[62] K. F. Evans and W. Wiscombe, "Improvements to the SHDOM radiative transfer modeling package," in *Proc. 13th ARM Sci. Team Meeting*, vol. 6, 2003, p. 8.
[63] P. Yang, K. N. Liou, K. Wyser, and D. Mitchell, "Parameterization of the scattering and absorption properties of individual ice crystals," *J. Geophys. Research: Atmos.*, vol. 105, no. D4, pp. 4699–4718, Feb. 2000.
[64] J. Gumbel *et al.*, "The MATS satellite mission—Gravity wave studies by mesospheric Airglow/Aerosol tomography and spectroscopy," *Atmos. Chem. Phys.*, vol. 20, no. 1, pp. 431–455, Jan. 2020.
[65] L. William, *Fundamentals Geophysics*. Cambridge, U.K.: Cambridge Univ. Press, 2007.
[66] D. B. Goldman, "Vignette and exposure calibration and compensation," *IEEE Trans. Pattern Anal. Mach. Intell.*, vol. 32, no. 12, pp. 2276–2288, Dec. 2010.
[67] A. Litvinov and Y. Y. Schechner, "Addressing radiometric nonidealities: A unified framework," in *Proc. IEEE Comput. Soc. Conf. Comput. Vis. Pattern Recognit. (CVPR)*, Jun. 2005, pp. 52–59.

Masada Tzabari received the B.A. degree in physics and atmospheric sciences and the M.Sc. and Ph.D. degrees from The Hebrew University of Jerusalem, Jerusalem, Israel, in 2010, 2013, and 2018, respectively.

She is currently a Post-Doctoral Researcher with the Hybrid Imaging Laboratory, Department of Electrical Engineering, Technion-Israel Institute of Technology, Haifa, Israel. Her research interests include natural phenomena and artificial applications of light transfer and polarization.

Vadim Holodovsky (Member, IEEE) received the M.Sc. degree in electrical engineering from Technion, Haifa, Israel, in 2016.

He is currently a Senior Research Associate with the Hybrid-Imaging Laboratory, Technion. His research interests include computer vision algorithms for 3-D retrievals and remote sensing. His work includes experiment designs, optics, cameras, polarization, and electronic hardware.

Omer Shubi received the B.Sc. degree in data science and engineering from the Technion-Israel Institute of Technology, Haifa, Israel, in 2021. He is currently pursuing the M.Sc. degree in data science with the Faculty of Industrial Engineering and Management, Technion, Haifa.

Eshkol Eytan received the B.Sc. degree in climate, atmospheric, and oceanography sciences from Hebrew University, Jerusalem, Israel, in 2016, and the M.Sc. degree in atmospheric science from the Weizmann Institute of Science, Rehovot, Israel, in 2018, where he is pursuing the Ph.D. degree with the Earth and Planetary Sciences Department.

His research interests include cloud physics, radiation transfer, and remote sensing, aerosol-cloud interactions, and clouds' role in Earth's energy budget.

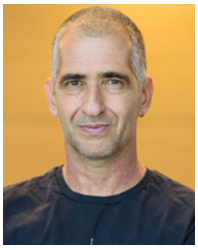

Ilan Koren received the Ph.D. degree in cloud physics from the Department of Geophysics and Planetary Sciences, Tel Aviv University, Tel Aviv, Israel, in 2002.

He then spent three years conducting postdoctoral research with the National Aeronautics and Space Administration (NASA) Goddard Space Flight Center's Climate and Radiation Branch before joining the Weizmann Institute of Science, Rehovot, Israel, in 2005. His research interests are in cloud and rain physics and ocean-atmosphere interactions. He explores theoretical aspects of complex systems and uses clouds and rain as a model to explore pattern formation and self-organizing systems.

Dr. Koren received the International Radiation Commission-Young Scientist Award in 2008 and the Krill Prize for Excellence in Scientific Research in 2009. He was a recipient of the two ERC Grants, in 2012 and 2019.

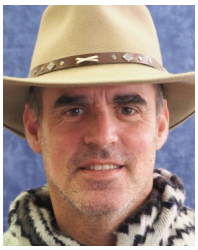

Yoav Y. Schechner (Member, IEEE) received the B.A. and M.Sc. degrees in physics and the Ph.D. degree in electrical engineering (EE) from the Technion-Israel Institute of Technology, Haifa, Israel, in 1990, 1994, and 2000, respectively.

Afterward, he was a Research Scientist with Columbia University (CS), New York, NY, USA. Since 2002, he has been a Faculty Member with the Technion's Viterbi Faculty of Electrical Engineering, Technion-Israel Institute of Technology. He is the Diane and Mark Seiden Chair in science. He is a Principal Investigator and the Coordinator of the CloudCT Project, funded by ERC. In 2010 and 2011 he was a Visiting Scientist with the California Institute of Technology (Caltech), Pasadena, CA, USA, and the NASA's Jet Propulsion Laboratory (JPL), La Cañada Flintridge, CA, USA. His research interests involve outdoor phenomena and all aspects of imaging.

Dr. Schechner received the Best Student Paper Award at the IEEE Conference on Computer Vision and Pattern Recognition (CVPR) in 2017, the Best Paper Awards at the IEEE International Conference on Computational Photography (ICCP) in 2013 and 2018, and the Distinguished Lecturer Award, Technion 2020. He was a recipient of the Ray and Miriam Klein Research Award, the Henry Taub Prize for Academic Excellence, the Otto Schwarz Foundation Excellence Award, and the Landau Fellowship.